

Diffusion MRI microstructure models with *in vivo* human brain Connectom data: results from a multi-group comparison

Uran Ferizi^{a,b,c,*}, Benoit Scherrer^{d,*}, Torben Schneider^{c,e,*}, Mohammad Alipoor^f, Odin Eufracio^g, Rutger H.J. Fick^h, Rachid Deriche^h, Markus Nilssonⁱ, Ana K. Loya-Olivas^g, Mariano Rivera^g, Dirk H.J. Poot^j, Alonso Ramirez-Manzanares^g, Jose L. Marroquin^g, Ariel Rokem^l, Christian Pötter^l, Robert F. Dougherty^l, Ken Sakaie^m, Claudia Wheeler-Kingshott^c, Simon K. Warfield^d, Thomas Witzelⁿ, Lawrence L. Waldⁿ, José G. Raya^b, Daniel C. Alexander^a

^aCentre for Medical Image Computing, University College London, UK

^bDepartment of Radiology, New York University School of Medicine, USA

^cDepartment of Neuroinflammation, Institute of Neurology, University College London, UK

^dComputational Radiology Laboratory, Boston Children's Hosp., Harvard University, USA

^ePhilips Healthcare, Guildford, Surrey, UK

^fChalmers University of Technology, Gothenburg, Sweden

^gCentro de Investigacion en Matematicas AC, Guanajuato, Mexico

^hAthena Project-Team, INRIA Sophia Antipolis - Méditerranée, France

ⁱLund University Bioimaging Center, Lund University, Sweden

^jErasmus Medical Center and Delft University of Technology, the Netherlands

^keScience Institute, University of Washington, USA

^lCenter for Cognitive and Neurobiological Imaging, Stanford University, USA

^mImaging Institute, The Cleveland Clinic, Cleveland, USA

ⁿA.A. Martinos Center for Biomedical Imaging, MGH, Harvard University, USA

Abstract

A large number of mathematical models have been proposed to describe the measured signal in diffusion-weighted (DW) magnetic resonance imaging (MRI). However, model comparison to date focuses only on specific subclasses, and little or no information is available in the literature on how performance varies among the different types of models. To address this deficiency we organized the “White Matter Modeling Challenge” during the International Symposium on Biomedical Imaging (ISBI) 2015 conference. This competition aimed to compare a range of different kinds of model in their ability to explain measured *in vivo* DW human brain data. We focus specifically on the challenge of explaining a large range of measurable data. We used the Connectome scanner at the Massachusetts General Hospital, using gradient strengths of up to 300 mT/m and a broad set of diffusion times. We focused on assessing the DW signal prediction in two regions: the genu in the corpus callosum, where the fibres are relatively straight and parallel, and the fornix, where the configuration of fibres is more complex. The challenge participants had access to three-quarters of the dataset, and their models were ranked on their ability to predict the remaining unseen quarter of the data. The challenge provided a unique opportunity for quantitative comparison of a diverse set of methods from multiple groups worldwide. The comparison of the challenge entries reveals important trends and conclusions that influence the next generation of diffusion-based quantitative MRI techniques. The first is that signal models do not necessarily outperform tissue models; in fact tissue models on average rank highest of those tested. The second is that assuming a non-Gaussian (rather than a purely Gaussian)

noise model provides little benefit. The third is that preprocessing the training data (here, omitting signal outliers) and using signal predicting strategies, such as bootstrapping or cross-validation, could benefit the model fitting. The analysis in this study provides a benchmark for other models and the data remains available to build up a more complete comparison over future years.

Keywords: diffusion MRI, model selection, Connectome, brain microstructure, genu, fornix

1. Introduction

Diffusion-weighted (DW) magnetic resonance imaging (MRI) can provide unique insights into the microstructure of living tissue and is increasingly used to study the microanatomy and development of normal functioning tissue as well as its pathology. Mathematical models for analysis and interpretation have been crucial for the clinical adoption of DW-MRI. Even though diffusion tensor imaging (DTI) (Basser et al., 1994), which is based on a simple model of the DW-MRI signal, has shown promise in clinical applications (Assaf and Pasternak, 2008), e.g. Alzheimer’s disease (Rose et al., 2000), Multiple Sclerosis (Werring et al., 2000) or brain tumors (Price et al., 2006), a much wider variety of DW-MRI models has been proposed to extract more information from the DW signal.

Models generally fall between two extremes of models of the tissue and models of the signal. Models of the tissue (Behrens et al., 2003, 2007; Assaf and Basser, 2005; Alexander et al., 2010; Dyrby et al., 2013; Sotiropoulos et al., 2012; Zhang et al., 2012; Scherrer et al., 2015; Kaden et al., 2016) explicitly describe the underlying tissue microstructure in each voxel with a multi-compartment approach (Stanisz et al., 1997; Panagiotaki et al., 2012; Nilsson et al., 2013). Models of the signal focus on describing the DW signal attenuation without explicitly describing the underlying tissue composition that gives rise to the signal (Liu et al., 2003; Tuch, 2004; Jensen et al., 2005a,b; Descoteaux et al., 2007; Assemlal et al., 2009; Yablonskiy and Sukstanskii, 2010; Kiselev, 2011; Özarlan et al., 2008, 2013). Other approaches fall between these two classes and include some features of the tissue, such as the distribution of fibre orientations, but often describe the signal from individual fibres without modelling the fibre composition explicitly (Mitra et al., 1992; Tournier et al., 2004; Alexander, 2005; Anderson, 2005; Jian and Vemuri, 2007; Jian et al., 2007; Sakaie and Lowe, 2007; Dell’Acqua et al., 2007; Jbabdi et al., 2012; Rathi et al., 2014; Kaden et al., 2015).

Despite this explosion of DW-MRI models, a broad comparison on a common dataset and within a common evaluation framework is lacking, so little is understood about which models are more plausible representations or explanations of the signal. Panagiotaki et al. (2012) established a taxonomy of diffusion compartment models and compared 47 of them using data from the fixed corpus callosum of a rat acquired

*Joint first co-authors

Email address: uran.ferizi@med.nyu.edu (Uran Ferizi)

on a pre-clinical system. Later, Ferizi et al. (2014) performed a similar experiment using data from a live human subject, while Ferizi et al. (2013, 2015) explored a different class of models that aim to capture fiber dispersion. Rokem et al. (2015) compared two classes of models using cross-validation and test-retest accuracy. All these studies (Panagiotaki et al., 2012; Ferizi, 2014; Rokem et al., 2015) aim to evaluate variations with specific classes of models with all other variables of the parameter estimation pipeline (i.e. noise model, fitting routine, etc.) fixed. While this provides fundamental insight into which compartments are important in compartment models, questions remain about the broader landscape of models; in particular, which classes of models explain the signal best and how strongly performance depends on the choice of parameter-estimation procedure.

Publicly organized challenges provide a unique opportunity to bring a research community together to gain a quantitative and unbiased comparison of a diverse set of methods applicable to a particular data-processing task. Such publicly organized challenges have helped to establish a common ground for the evaluation of competing methods in a variety of imaging-related tasks, e.g. registration of MRI brain images (Klein et al., 2009), diagnostic group classification for dementia using structural MRI (Bron et al., 2015), tissue segmentation on brain (Mendrik et al., 2015) and prostate tissue (Litjens et al., 2014), on CT images for thoracic tissue (Murphy et al., 2011), carotid tissue (Hameeteman et al., 2011), and breathing airways tissue (Lo et al., 2012), fetal ultrasound images (Rueda et al., 2014), or particle tracking (Chenouard et al., 2014) have been organized. In DW-MRI, public challenges have focused on recovering synthetic intra-voxel fibre configurations (Daducci et al., 2014) or evaluating tractography techniques (Fillard et al., 2011; Pujol et al., 2015) and have been very successful at driving research and translation forward. Another interesting comparison of reconstruction methods using DW-MRI data was based on signal acquired from a physical phantom (Ning et al., 2015).

Here we report on such a community-wide challenge to model the variation of DW-MRI signals at the voxel level in the *in vivo* human brain. Modelling the diffusion signal is a key step in realising practical and reliable quantitative imaging techniques based on diffusion MRI. The challenge in the area is to extract the salient features from the diffusion signal and relate them to the principal features of the underlying tissue (e.g., in the case of brain white matter, the fibre orientation, axonal packing and axonal size). Three distinct questions arise: i) given the richest possible dataset that samples the space of achievable measurements as widely as possible, which mathematical model can capture best the intrinsic variation of the acquired signal; ii) which tissue features can be derived from the model; iii) what subset of those features can we estimate from limited acquisition time on a standard clinical scanner and what dataset best supports such estimates? The intuition gained from (i) is generalisable over a wide range of applications, while (ii) and (iii) are highly dependent on the MRI study design and the available hardware. Therefore, our challenge focuses on question (i), as an understanding of (i) is necessary to inform (ii) and (iii). To that end, we acquire the richest possible dataset using the most powerful hardware available and the most motivated subject available

(UF). Specifically, we use the Connectome scanner (Setsompop et al., 2013), which is unique among human scanners in having 300 mT/m gradients, rather than 40 mT/m typical of state-of-the-art human scanners. Preclinical work by Dyrby et al. (2013) highlights the benefits of such strong gradients and the first results from the Connectome scanner (McNab et al., 2013; Duval et al., 2014; Ferizi et al., 2015; Huang et al., 2015) are now starting to verify those findings.

The uniquely rich dataset from Ferizi et al. (2015), acquired on the Connectome system, samples around five thousand points in the space of possible measurements from a standard Stejskal-Tanner DW-MRI sequence. Each DWI has a unique combination of gradient strength, diffusion time, pulse width and echo time; i.e. they vary all the key parameters of the sequence to highlight sensitivity to as many underlying tissue properties as possible. This offers a unique opportunity for the comparison of the many different types of models within a common framework, over a very wide range of the measurement space. Using this rich dataset we organized the White Matter Modeling challenge, held during the 2015 International Symposium on Biomedical Imaging (ISBI) in New York. The goal of the challenge was to evaluate and compare the models in two different tissue configurations that are common in the brain: 1) a white matter region of interest where fibers are relatively straight and parallel, specifically, the genu of the corpus callosum; and 2) a region in which the fiber configuration is more complex, specifically, the fornix. Challenge participants had access to three-quarters of each whole dataset; the participating models were evaluated on how well they predicted the remaining ‘unseen’ part of the data. This kind of model comparison, based on prediction error, is a common and crucial part of the development of any statistical model-based estimation applications. Books such as ? explain how and why such comparisons should be performed to reject models that are theoretically plausible but that the data do not support. As announced before the challenge, the final ranking was based exclusively on the performance on the genu data. In this paper, however, we include results from both the genu and the fornix.

The challenge entries include a wide range of different kinds of model and estimation procedure. In contrast to earlier model comparisons (Panagiotaki et al., 2012; Ferizi, 2014; Rokem et al., 2015), the results provide new insight into which broad classes of model explain the signal best and what features of the estimation procedure are important. Although the sampling of the set of possible techniques is necessarily sparse, as any model could in theory combine with any estimation procedure and each has many variables, the results provide some surprising and key insights into the benefits of different approaches. This information is very timely, as recent model-based diffusion MRI techniques, such as NODDI (Zhang et al., 2012), SMT (Kaden et al., 2015, 2016), DIAMOND (Scherrer et al., 2015), DKI (Fieremans et al., 2011) and LEMONADE (Novikov D, 2015), are starting to become widely adopted in clinical studies and trials. Despite their success, intense debate continues in the field about applicability of different models and fitting routines (Jelescu et al., 2015, 2016). The insights from this challenge provide key pointers to the important features of the next-generation of front-line imaging techniques of this type. Moreover, the data

and evaluation routines remain available to form the basis of an expanding ranking of models and fitting routines and a standard yardstick for future model development.

The paper is organized as follows. We first describe in section 2 the experimental protocol, data post-processing and preparation of the training and testing data. We then present the methods for ranking the models and tabulate succinctly the various models involved in the competition. We report the challenge results in section 3 and discuss these results in section 4; a more detailed description of the models follows in the Appendix, section 7.

2. Material and Methods

2.1. The complete experiment protocol

One healthy volunteer was scanned over two non-stop 4h sessions. The imaged volume comprised twenty 4mm-thick whole-brain sagittal slices covering the corpus callosum left-right. The image size was 110 x 110 and the in-plane resolution 2 x 2 mm². Forty-five unique and evenly distributed diffusion directions (taken from <http://www.camino.org.uk>) were acquired for each shell, with both positive and negative polarities; these directions were the same in each shell. We also included 10 interleaved b=0 measurements, leading to a total of 100 measurements per shell. Each shell had a unique combination of $\Delta = \{22, 40, 60, 80, 100, 120\}$ ms, $\delta = \{3, 8\}$ ms, and $|\mathbf{G}| = \{60, 100, 200, 300\}$ mT/m (see Table 1). The measurements were randomized within each shell, whereas the gradient strengths were interleaved. We visually inspected the images and have not observed any obvious shifts from gradient heating. The minimum possible echo time (TE) for each gradient duration and diffusion time combination was chosen to enhance SNR for shorter diffusion times, and potentially enables estimation of compartment-specific relaxation constants. The SNR of b = 0 images was 35 at TE = 49 ms and 6 at TE = 152 ms. To find the SNR we used the background signal, as well as the signal noise floor in b = 0 images i.e. the residual signal along the fibres at the highest b-value. In both cases these estimates matched reasonably well. More details about the acquisition protocol can be found in Ferizi et al. (2015).

2.2. Post-processing

All post-processing was performed using FSL (Jenkinson et al., 2002). The DW images were corrected for eddy current distortions separately for each combination of δ and Δ using FSL's *Eddy* module (www.fmrib.ox.ac.uk/fsl/eddy) with its default settings. The images were then co-registered using FSL's *Fnirt* package. As the 48 shells were acquired across a wide range of TEs, over two days, we chose to proceed in two steps. First, within each quarter of the dataset (different day, different δ) we registered all the b=0 images together. We then applied these transformations to their intermediary DW images, using a tri-linear resampling interpolation. The second stage involved co-registering the four different quarters. To help the

co-registration, especially between the two days’ images which required some through-plane adjustment as well, we omitted areas of considerable eddy-current distortions by reducing the number of slices from 20 to 5 (that is, leaving two images either side of the mid-sagittal plane) and reducing the in-plane image size to 75x80.

2.3. Training and testing data

The data for this work originated from two ROIs, each containing 6 voxels (see Fig. 2). The first ROI was selected in the middle of the genu in the corpus callosum, where the fibres are mostly straight and coherent. The second ROI’s fibre configuration is more complex: it lies in the body of fornix, where two bundles of fibers bend and bifurcate.

The dataset was split into two parts: the training dataset and the testing dataset. The training dataset was fully available for the challenge participants. The testing dataset was retained by the organisers. The DW signal of the training dataset (36 shells, with acquisition parameters shown in black in Table 1) was provided together with the gradient scheme on the challenge website (<http://cmic.cs.ucl.ac.uk/wmmchallenge/>). This data was used by the participants to estimate their DW-MRI model parameters. The signal attenuation in the testing dataset (12 shells, with acquisition parameters shown in red in Table 1) was kept unseen. Participants were then asked to predict the signal for the corresponding gradient scheme. The challenge participants were free to use as much or as little of the training data provided to predict the signal of the test dataset for the six voxels in each ROI.

Figure 4 shows the DW signal attenuation for each shell in the genu dataset, with stars in the legend indicating which shells were left out for testing. In this plot, a small number of data appear as ‘outliers’ (two such data are shown with arrows in the bottom-left subplot of Figure 4). Specifically, we counted about 10 of them among more than 4812 measurements, most of them being in the $b=300$ s/mm² shell. Since these outliers appear to be specific to the $b=300$ s/mm² shell, and not in other shells with similar b-value, we attribute them to a momentary twitching of the subject rather than more systematic affects, such as perfusion. Similarly, figure 6 shows the signal for the fornix region, with the signal over the six voxels averaged out.

2.4. Models ranking

Models were evaluated and ranked based on their ability to accurately predict the unseen DW signal. Specifically, the metric used was the sum of square differences between the hidden signal and the predicted signal, corrected for Rician noise (Jones and Basser, 2004):

$$SSE = \sum_{i=1}^N \frac{(\tilde{S}_i - \sqrt{S_i^2 + \sigma^2})^2}{\sigma^2} \quad (1)$$

where N is the number of measurements, \tilde{S}_i is the i -th measured signal, S_i its prediction from the model, and σ is the noise standard deviation.

2.5. Competing models

We give in this section a short summary of competing models in the challenge. Additionally, Table 2 provides a summary of the key characteristics of the competing models. A more detailed description of each model is included in the Appendix, section 7.

- *Ramirez-Manzanares*: A dictionary-based technique that accounts for multiple fibre bundles, and models the distribution of tissues properties (axon radius, parallel diffusivity) and the orientation dispersion of fibres.
- *Nilsson*: A multi-compartment model that models isotropic, hindered and restricted diffusion, and accounts for varying (T_1 , T_2) relaxation times for each compartment (Nilsson et al., 2012).
- *Scherrer*: A multi-compartment model in which each compartment is modelled by a statistical distribution of 3-D tensors (Scherrer et al., 2015)
- *Ferizi₁ and Ferizi₂*: Two three-compartment models that account for varying T_2 relaxation times for each compartment. As regards the intracellular compartment, Ferizi₁ models the orientation dispersion by using dispersed sticks as one compartment; Ferizi₂ uses a single radius cylinder instead (Ferizi et al., 2015).
- *Poot*: A 3-compartment model comprising an isotropic diffusion compartment, a tensor compartment, and a model-free compartment in which an ADC is estimated for each direction independently. T_2 relaxation times are also estimated for each compartment (Poot and Klein., 2015).
- *Rokem*: A combination of the sparse fascicle model Rokem et al. (2015) with restriction spectrum imaging White et al. (2013) that describes the signal arising from a multi-compartment model in a densely sampled spherical grid, using L1 regularization to enforce sparsity.
- *Eufracio*: An extension of the Diffusion Basis Function (DBF) model that accounts for multiple b-value shells.
- *Loyas-Olivas₁ and Loyas-Olivas₂*: Two models based on the Linear Acceleration of Sparse and Adaptive Diffusion Dictionary (LASADD) technique. Loyas-Olivas₁ uses the DBF signal model, while Loyas-Olivas₂ uses a three-compartment tissue model. The optimization uses linearized signal models to speed up computation and sparseness constraints to regularise.
- *Alipoor*: A model of fourth-order tensors, corrected for T_2 -relaxation across different shells. A robust LS fitting was applied to mitigate influence of outliers.

- *Sakaie*: A two-compartment model of restricted and hindered diffusion with angular variation. A simple exclusion scheme based on the $b=0$ signal intensity was applied to remove outliers.
- *Fick*: A spatio-temporal signal model to simultaneously represent 3-D diffusion signal over varying diffusion time. Laplacian regularization was applied during the fitting (Fick et al., 2015).
- *Rivera*: A regularized linear regression model of diffusion encoding variables. This is intentionally built as a simplistic model to be used as a baseline for model comparison.

3. Results

Figure 8 shows the averaged prediction error in each ROI (top subplot is for the genu, bottom subplot is for the fornix) and the corresponding overall ranking of the participating models in the challenge. The first six models in the genu ranking performed similarly, each higher ranked model marginally improving on the prediction error. The prediction error clearly increased at a higher rate for the subsequent models. In the fornix dataset, the prediction error was higher than in the genu. For both datasets the first six models were the same, albeit permuted. Most of the models performed similarly in terms of ranking in both genu and fornix cases, i.e. Nilsson (2nd in genu/1st in fornix), Scherrer (3rd/2nd) and Ferizi_2 (4th/4th). Others performed significantly better in one of the cases, with Ramirez-Manzanares (1st/6th) being the most notable.

Figure 8 also details the prediction error for different ranges of b -values in the unseen dataset. Models inevitably vary in their prediction capabilities; some models perform better within a given b -value range but are penalised more in another. Across the models, as the figure shows, the ranking between models was dominated by the signal prediction accuracy for b -values between 750 and 1400 s/mm^2 ; specifically, the shell which has the largest weight on this error is the $b=1100 \text{ s}/\text{mm}^2$ one. The top-ranking models, nevertheless, were better at predicting the signal for higher b -value images as well. The prediction performance of lower b -value images ($<750 \text{ s}/\text{mm}^2$) in the genu was less consistent across ranks. For example the models of Rokem and Sakaie outperformed most of the higher ranking models in this low b -value range. The fornix is a more complex region than the genu, hence the performance across the shells is less consistent. In the fornix the prediction errors were generally larger than in the genu across all b -values for all models, except Rivera's, which showed the opposite. The prediction errors of the $b = 0$ images were also larger than in the genu, especially for the highly ranked models of Poot and Ferizi. The prediction errors in other b -value shells followed more closely the overall ranking of the models.

Figure 10 shows the prediction error for each voxel independently. In the genu plot, the best performing models had high consistency of low prediction errors across all individual voxels. These were followed by the models with consistent larger prediction error in all voxels. Most of the lowest ranking models not only had

largest prediction errors, they also showed large variations in prediction performance. For example, while the model of Loya-Olivas_2 was competitive in voxel 5, it ranked low due to large prediction errors in voxel 4 and voxel 6. The results in the fornix show a lower consistency of prediction errors between the voxels than in the genu. Specifically, two voxels (3 and 4) showed substantially larger prediction errors and were likely responsible for much of the overall ranking.

Finally, we report in figures 12 and 14 an illustration of the quality of fit of each model to 4 representative shells, including the $b=1100$ s/mm² shell mentioned above.

4. Discussion

The challenge set out to compare the ability of various kinds of models to predict the diffusion MR signal from white matter over a very wide range of measurement parameters – exploring the boundaries of possible future quantitative diffusion MR techniques. The fourteen challenge entries were a good representation of the many available models that are proposed in the literature. They also use a variety of fitting routines, and so provide additional insight into the effects of algorithmic choices during parameter estimation. Although the set of methods tested is not sufficient to make a full comparison of each independent feature (diffusion model, noise model, fitting routine, etc.), and the number of combinations prohibits an exhaustive comparison, the results of the challenge do reveal some important trends.

4.1. Main conclusions

The first insight is on the type of model used. Signal models do not necessarily outrank tissue models; indeed, models of the signal (Alipoor, Sakaie, Fick, Riviera) ranked on average lower than models of the tissues with our dataset, despite their theoretical ability to offer more flexibility in describing the raw signal. This is quite surprising, as the current perception within the field is that, generally, we can capture the signal variation much better through a functional description of the signal (signal models) rather than via a biophysical model of the tissue (tissue models). The former generally consist of bases of arbitrary complexity, whereas the latter are generally very parsimonious models that rely on extremely crude descriptions of tissue (e.g. white matter as parallel impermeable cylinders). The results suggest that the flexibility of signal models can rapidly lead to over-fitting. However, the tissue models can explain the signal relatively well even with just a few parameters (compare the quality-of-fit plots of the Rivera model in figure 14 to the signal prediction of the top models in figure 12; the higher the b-value, the worse the prediction of the linear signal model). Certain underlying assumptions may cause the signal models to perform less well than expected. For example, they are often designed to work with data with a single diffusion time and do not generalise naturally to incorporate the additional dimension (although see Fick et al. (2015) for some steps towards generalisation). Many of the tissue models on the other hand naturally account for finite δ , varying diffusion times and gradient strength (e.g. the Ramirez-Manzanares, Nilsson and Ferizi models in our collection).

The second insight concerns the choice of noise modelling. Assuming a non-Gaussian noise model, as used by three models, provides little benefit over a Gaussian assumption. This is likely because much of the data has high SNR. Although signal levels at high b-values do often hit the noise floor, the magnitude of the noise floor is small compared to signals at moderate b-values. In this challenge most participants used non-linear least-squares or maximum likelihood optimisation. Additional regularisation of the objective function (Eufrazio&Rivera/Lasso, Rokem/Elastic Net, Fick/Laplacian) appeared to have little benefit over non-regularised optimization.

The third observation is about removing signal outliers. Five of the eleven models preprocessed the training data by clearing out outliers, including the top two models. We tried this procedure with two good models which did not use such a procedure, Ferizi₁ and Ferizi₂, and observed that it did not affect the ranking, though it did marginally improve the prediction error. This is understandable considering the relative little weight these apparent outliers have on the total number of measurements (10 points from a 4812-strong dataset). Additionally, specific strategies for predicting signal, e.g. bootstrapping or cross-validation, as used by the top two models of Ramirez-Manzanares and Nilsson, may also help the model ranking.

4.2. Limitations and future directions

Although this challenge provides several new insights into the choice of model and fitting procedure for diffusion-based quantitative imaging tools, it has a number of limitations that future challenges might be designed to address. One limitations of the study is that we use a very rich acquisition protocol that is not representative of common or clinical acquisition protocols. In particular, we cover a very wide range of b-values and the data acquisition (protocol) we use consists of many TEs unlike many other multi-shell diffusion datasets that use a fixed TE. As stated in the Introduction, our intention is to sample the measurement space as widely as possible to support the most informative models possible. Varying the TE makes it possible to probe compartment-specific T_2 (whose decay Ferizi et al. (2015) finds to be monoexponential at the voxel level), an investigation which would be impossible with a single TE. However, the good performance of DIAMOND also shows that a model with fixed δ and Δ could be used with multi-TE datasets, and that, while the majority of the full data was ignored in each of the reconstructions, its prediction error compared favourably with other techniques.

We use the unique human Connectome scanner (Setsompop et al., 2013) to acquire a dataset with gradients of up to 300 mT/m, which is not readily available in most current MR machines. However, previous preclinical work by Dyrby et al. (2013) suggests that high diffusion gradients enrich the signal, which helps model fitting and comparison. Future challenges might be designed that focus on explaining the signal and estimating parameters from data more typical of clinical acquisitions.

Assessing the prediction performance on unseen data as in this challenge is different from assessing the

fitting error: it implicitly penalises models which overfit the data. However, since most of the missing shells lie in-between other shells (in terms of b-values, TEs, etc.), the quality of signal extrapolation was not assessed. We get a glimpse of this from figure 8, where the SSE is unevenly distributed between the b-values. Here, the shell which bore the largest error is the $b=1100$ s/mm² one; see also figures 12 and 14. Of all “unseen” shells, this shell combines the lowest Δ and highest $|G|$, placing it on the edge of the range of the measurement space sampled. Such a b-value shell combines high signal magnitude with high sensitivity (i.e. the gradient of signal against b-value is highest in this range), which makes it hard to predict. Future work can take this further, by selecting unseen shells outside of the min-max range of experimental parameters. This is likely to penalise more complex models that overfit the data even more strongly.

We did not take into account the computational demand of each model, and this might limit the generalisation of the results. Models that use bootstrapping generally have a higher computational burden and may not be feasible for large datasets, e.g. whole brain coverage.

The dataset used in this challenge is specific to one subject who underwent a long duration acquisition, which adds to the question of the generalisability. The subsequent preprocessing of the data is also a factor to bear in mind: the registration of two 4h datasets, across such a broad range of echo times, poses its own challenges for certain non-homogenous regions in the brain, such as the fornix (as compared with, for example, the relatively large genu). Thus the results may be somewhat subject specific and may be affected by residual alignment errors.

Another limitation is that we only look at isolated voxels inside the corpus callosum and the fornix. Questions still remain about which models are viable even in the most coherent areas of the brain with the simplest geometry so we believe our focused challenge on well-defined areas is an informative first step necessary before extending the idea to the whole of white matter, which would make for an extremely complex challenge. We note however, recent work by Ghosh et al. (2016) that illustrates such an approach with Human Connectome Project (HCP) data.

We focused here on comparing models based on their ability to predict unseen data. Although models that reflect true underlying tissue structure should explain the data well, we cannot infer in general that models that predict unseen data better are mechanistically closer to the tissue than those that do not. As we discuss in the introduction, the main power of evaluating models in terms of prediction error is to reject models that cannot explain the data. Thus, while the identification of parsimonious models that explain the data certainly has great benefit, further validation is necessary through comparison of the parameters that they estimate with independent measurements, e.g. obtained through microscopy (our challenge makes no attempt to assess the integrity of parameter estimates themselves, but future challenges might use such performance criteria). We note however that major difficulties arise in obtaining ground truth in realistic samples. In particular, histology does not provide a perfect ground truth for assessing quantitative non-invasive techniques. There are two good reasons for this: a) the histological preparation process disrupts

the tissue from its in-vivo state and b) certain parameters simply cannot be measured histologically, e.g. diffusivity and permeability. Moreover, the results from this study do not immediately translate into the ability of estimated models to provide useful information about the WM microstructure integrity, such as the presence of axonal loss, demyelination or oedema in abnormal tissue. Specifically for tissue models, obtaining a direct histological analogue is often difficult. One good example of this are models that incorporate an axonal radius parameter, known to generally overestimate the true axonal radius, as discussed in detail e.g. by Barazany et al. (2009), Alexander et al. (2010) and Dyrby et al. (2013).

5. Conclusion

Challenges such as this have great value in bringing the community together and provide unbiased comparison of wide ranging solutions to key data-processing problems. They raise new insights and ideas motivating more directed future studies. The data is publicly available for others to use, with more details of the dataset given on the Challenge website <http://cmic.cs.ucl.ac.uk/wmmchallenge/>. On this website, an up-to-date ranking of the models will be available too, where additional models can be added after the publication of the article. This will provide an important yardstick for future models and parameter estimation routines.

6. Acknowledgements

Research reported in this manuscript was supported by:

- EPSRC supported this work through grants EP/G007748, EP/L022680/1, EP/I027084/01, EP/M020533/1 and EP/N018702/1.
- U. Ferizi is also supported by the National Institute of Arthritis and Musculoskeletal and Skin Diseases (NIAMS) of the National Institute of Health (NIH) under award numbers R21AR066897 and RO1AR067789.
- B. Scherrer was supported in part by NIH R01 NS079788, R01 EB019483, R01 EB018988 and BCH TRP Pilot and BCH CTREC K-to-R Merit Award.
- M. Nilsson is supported by the Swedish Strategic Research (SSF) Grant AM13- 0090

The content is solely the responsibility of the authors, and does not necessarily represent the official views of the funding bodies (EPSRC or NIH).

Lastly, we would like to thank ISBI 2015 challenge organisers, in particular, Stephen R. Aylward (Kitware Inc., USA) and Badri Roysam (University of Houston, USA).

7. Appendix: Competing models

7.1. Tissue models

7.1.1. Ramirez-Manzanares (CIMAT, Mexico): Empirical Diffusion-and-Direction Distributions (ED³)

This work builds on the statistical modelling of the apparent diffusion coefficient (Yablonskiy et al., 2003), and tackles the modelling of axon fiber dispersion in single (Axer et al., 2001; Zhang et al., 2012) and multiple fibre bundle cases. The method empirically estimates (rather than imposes) the distribution of tissue properties (axon radius, parallel diffusion, etc.), as well as the orientational distribution of the bundles. The general framework is as follows:

- estimation of mean principal diffusion directions (PDD) per axon bundle;
- selection of a dense set of orientationally-focused basis directions that capture the discrete non-parametric fiber dispersion;
- design of a dictionary of intra/extra cellular synthetic DW-signals which are precomputed along the basis directions (see the DBF method in Ramirez-Manzanares et al. (2007));
- computation of the size compartments per diffusion atom of the dictionary (model fitting).

The PDDs are estimated from the DT (single bundle case) and DBF (Ramirez-Manzanares et al., 2007) (complex structure cases). The 120 orientations closest to the PDDs are selected from a set of 1000, evenly distributed orientations. The intra axonal signals S^i are precomputed from the model in Van Gelderen et al. (1994) for restricted diffusion within a cylinder with radius $R = 1, 2, \dots, 10 \mu m$ and parallel diffusion $d_{\parallel} = 1, 1.1, \dots, 2.1 \mu m^2/ms$. The extra-axonal signals are generated as: S^e from *zeppelins* with combinations of parallel and radial diffusion, $d_{\parallel} = 1, 1.1, \dots, 2.5 \mu m^2/ms$ and $d_{\perp} = 2, 3, \dots, 8 \mu m^2/ms$, the isotropic diffusion compartment signals $S_i^{iso} = \exp^{-q\tau d_{iso}}$ for $d_{iso} = 2, 2.1, 2.2, \dots, 4 \mu m^2/ms$, and the *dot* signal that takes into account static proton density. The values of the dictionary-atoms above were tuned by cross validation (Stone, 1974). The size compartments $\beta \geq 0$ computed in the weighted non-negative LS formulation:

$$\left\| W \left(S - S_0^{TE} \left(\sum_{i=1}^{N_i} \beta_i^i S_i^i - \sum_{j=1}^{N_e} \beta_j^e S_j^e - \sum_{k=1}^{N_{iso}} \beta_k^{iso} S_k^{iso} + \beta_{dot} \right) \right) \right\|_2^2 \quad (2)$$

indicate the atoms that explain the signal, the W weights are proportional to SNR. Overfitting is reduced by a *bootstrap* (Efron, 1979) procedure.

The cross-validation experiments indicate that the reconstructions given by the robust fitting of this rich multi-compartment diffusion dictionary allows to accurately predict non acquired MR signals for different machine protocols. This is of most interest in the development of methods able to detect the complex microstructure heterogeneity associated with the different compartments within the voxels. The atoms

with coefficients $\beta > 0$ depict the empirical distributions, and their orientations indicate non-parametrical bundle–dispersion configurations (as fanning or radially symmetrical). The recovered distributions reveal, for instance, the presence of axon radius only among 1 and 4 μm . One should take into account, however, that since the heterogeneous intra/extra-axonal T2 relaxation feature is not explicitly modeled, the method may compensate T2 variations by using, for instance, large isotropic d_{iso} coefficients to accurately fit the signal. For this reason, a direct interpretation of the fitted parameters may be misleading. The use of more specific models is a part of ongoing work.

7.1.2. Nilsson (Lund, Sweden) : Multi-compartment model outlier rejection and separate fitting of b_0 data

This multiple compartment model was developed specifically for the ISBI WM challenge and built up by a relaxation-weighted and time-dependent diffusion tensors according to

$$S = S_0 \sum_i w_i e^{-\mathbf{B}:\mathbf{D}_i} e^{-TE/T2_i} \left(1 - e^{-(TR-TE/2)/T1_i} \right) \quad (3)$$

where $\mathbf{B} = b\vec{n}^{\otimes 2}$ and $b = (\gamma\delta g)^2 t_d$. The diffusion time t_d was corrected for rise times (ξ) according to $t_d = \Delta - \delta/3 + \xi^3/30\delta^2 - \xi^2/6\delta$. Each component was also described by a weight (w_i) and relaxation times ($T1_i$ and $T2_i$). The model featured three types of components, with either isotropic, hindered and restricted diffusion. Diffusion in the isotropic component was modeled by a single diffusion coefficient. The hindered and restricted components were modeled by cylinder-symmetric tensors described by axial and radial diffusivities together with the polar and azimuth angles. In the restricted component, the apparent diffusion coefficient of the radial component depended on δ and Δ , as well as on the cylinder radius, according to Vangelder et al. (1994).

Three modifications were performed to this very general model. First, to accommodate for potential bias in the b_0 images (which was the case for fornix data where deviations of up to 20σ was observed), the prediction for b_0 data was obtained from the median of all signals acquired with identical TE instead of from eq. 3. Second, opposite direction acquisitions were rescaled by a free model parameter, in order to allow for potential gradient instabilities inducing differences between the directions and their opposite directions. Third, models were generated dynamically during fitting by randomly selecting up to four hindered components and up to three restricted components. One isotropic component was always included.

The model was first fitted to half of the diffusion-weighted data (randomly selected), after which outliers were rejected ($> 2.5\sigma$). Thereafter a second fit was performed. Both fit steps assumed Gaussian noise and utilized the 'lsqcurvefit' function in Matlab. The procedure was repeated 100 times for different randomly generated models.

To prepare for submission of the results, only the models that best predicted the hidden half of the data was selected, after which the median of the selected predictions were used for the final prediction.

7.1.3. Scherrer (Harvard, USA): Distribution of anisotropic microstructural environments in diffusion compartment imaging (DIAMOND)

DIAMOND models the set of tissue compartments in each voxel by a finite sum of unimodal continuous distributions of diffusion tensors. This corresponds to a hybrid tissue model that combines biophysical and statistical modeling. As described in (Scherrer et al., 2015), the DW signal S_k for a gradient vector \mathbf{g}_k and b-value b_k is modeled by: $S_k = S_0 \left[\sum_{j=0}^N f_j \left(1 + \frac{b_k \mathbf{g}_k^T \mathbf{D}_j^0 \mathbf{g}_k}{\kappa_j} \right)^{-\kappa_j} \right]$, where S_0 is the non-attenuated signal, N is the number of compartments, f_j the relative fraction of occupancy of the j^{th} compartment and κ_j are \mathbf{D}_j^0 are respectively the concentration and the expectation of the j^{th} continuous tensor distribution. DIAMOND enables assessment of compartment-specific diffusion characteristics such as the compartment FA (cFA), the compartment RD (cRD) and the compartment MD (cMD). It also provides a novel measure of microstructural heterogeneity for each compartment.

The estimation of a continuous distribution of diffusion tensors requires DW data acquired with same timing parameters δ and Δ (Scherrer et al., 2015). To compare DIAMOND to other models on this dataset, we fitted separately one DIAMOND model for each $\{\delta, \Delta\}$ group (*i.e.*, for each TE group), leading to 12 DIAMOND models. One shell was missing in each TE group; we predicted its signal using the corresponding DIAMOND model. The model estimation was achieved as follows. We first computed the mean and standard deviation of S_0 (μ_{S_0} and σ_{S_0}) within each TE group and discarded DW-signals whose intensity were larger than $\mu_{S_0} + 3\sigma_{S_0}$ (simple artefact correction). We then estimated DIAMOND parameters as described in Scherrer et al. (2015), considering Gaussian noise and cylindrical anisotropic compartments. For the genu we considered a model with one freely diffusing and one anisotropic compartment; for the fornix we considered a model with one freely diffusing compartment and two anisotropic compartments.

7.1.4. Ferizi_1 and Ferizi_2 (UCL, England)

This submission uses two three-compartment models, as described in previous studies (Ferizi et al., 2014, 2013). These models consist of: 1) either a Bingham distribution of sticks or a Cylinder for the intracellular compartment; 2) a diffusion tensor for the extracellular compartment; 3) an isotropic CSF compartment. The T_2 relaxation element is fitted beforehand, to the (variable echo time) $b=0$ measurements. The signal model is:

$$S = \tilde{S}_0 \left(f_i \exp\left(-\frac{TE}{T_2^i}\right) S_i + f_e \exp\left(-\frac{TE}{T_2^e}\right) S_e + f_c \exp\left(-\frac{TE}{T_2^c}\right) S_c \right) \quad (4)$$

where f_i , f_e and f_c are the weights of the intracellular, extracellular, and third normalised compartment signals S_i , S_e and S_c , respectively; the values of compartmental T_2 are indexed similarly; \tilde{S}_0 is the proton density signal (which is TE-independent, and obtained from fitting to the $b = 0$ signal). These models, as shown in the figure below, emerged from previous studies (see references below). Here, however, a single white matter T2 and separate compartmental diffusivities are additionally fitted.

There is a two-stage model fitting procedure. The first step estimates the T2 decay rate of tissue, separately in each voxel, by fitting a bi-exponential model to the $b=0$ intensity as a function of TE, in which one component is from tissue and the other from CSF. A preliminary analysis of voxels fully inside WM regions shows no significant departure from mono-exponential decay, equal T2 are then assumed within the intra and extracellular compartments. When fitting the bi-exponential model, the value of T2 in CSF is fixed to 1,000ms (a more precise value of CSF is unlikely to be estimated with this protocol). Thus, for each voxel, the volume fraction of CSF, the \tilde{S}_0 and the T2 of the tissue are estimated. These three estimates are then fixed for all the subsequent model fits. Then, each model is fitted using the Levenberg-Marquardt algorithm with an offset-Gaussian noise model.

7.1.5. Poot (Erasmus, the Netherlands)

This submission uses a three compartment model, with for each compartment a different complexity of the diffusion model and an individual T_2 value. This model was developed specifically for the ISBI WM challenge and is the result of iteratively visualizing different projections of the residuals and trying to infer the maximum complexity that the rich data supports.

The first compartment models isotropic diffusion and, through the initialization procedure, it captures the fast diffusion components. The second compartment is modelled by a second order (diffusion) tensor and models intermediate diffusion strengths. The third compartment is model-free as the ADC is estimated for each direction independently. Each compartment additionally has an individual T_2 value and signal intensity at $b = 0$, $TE = 0$ (which could easily be translated into volume fractions). Hence, the complete model of a voxel in image j is given by

$$S_j(\boldsymbol{\theta}) = \sum_{i=1}^3 A_i e^{-TE_j R_{2,i}} e^{-b_j ADC_{j,i}} = \sum_{i=1}^3 e^{\mathbf{M}_{i,j} \boldsymbol{\theta}} \quad (5)$$

where S_j is the predicted signal intensity of image j , A_i is the non-diffusion weighted signal intensity of compartment i at zero TE , TE is the echo time, R_2 is the reciprocal of the T_2 relaxation time of compartment i , $b = (\Delta - \delta/3)\delta^2|G|^2\gamma^2$, with $\gamma = 42.5781\text{MHz/T}$, $ADC_{j,1} = c$, $ADC_{j,2} = \mathbf{g}_j^T \mathbf{D} \mathbf{g}_j$, $ADC_{j,3} = \mathbf{d} \mathbf{h}_j^T$, where \mathbf{d} is a vector with the ADC value of each orientation group and \mathbf{h}_j is a vector that selects the orientation group to which image j belongs (90 groups in total). Note that \mathbf{h}_j has at most one nonzero element and that element has a value of one. As displayed in the right most part of Eq.(5), the model can be written as a multiplication of matrices \mathbf{M}_i , containing all rows $\mathbf{M}_{i,j}$, with $\boldsymbol{\theta} = [\ln A_1, R_{2,1}, c, \ln A_2, R_{2,2}, D_{11}, D_{12}, D_{13}, D_{22}, D_{23}, D_{33}, \ln A_3, R_{2,3}, \mathbf{d}]^T$, which combines all 103 parameters into a single parameter vector. All parameters are simultaneously estimated from the provided 3311 measurements per voxel by a maximum likelihood estimator that assumes a Rician distribution of the measurements and simultaneously optimizes the noise level (Poot and Klein., 2015). The exact initialization and details of the optimization procedure are provided in the online supporting material. Finally, the signal

intensities of the ‘unseen’ data are predicted by substituting the estimate into Eq. (5).

7.1.6. Rokem (Stanford, USA): A restriction spectrum sparse fascicle model (RS-SFM)

The Sparse Fascicle Model, SFM (Rokem et al., 2015), is a member of the large family of models that account for the diffusion MRI signal in the white matter as a combination of signals due to compartments corresponding to different axonal fiber populations (fascicles), and other parts of the tissue. Model fitting proceeds in two steps. First, an isotropic component is fit. We model the effects of both the measurement echo time (TE), as well as the measurement b-value on the signal. These are fit as a $\log(TE)$ -dependent decay with a low order polynomial function, and a b-value-dependent multi-exponential decay (including also an offset to account for the Rician noise floor). The residuals from the isotropic component are then deconvolved with the perturbations in the signal due to a set of fascicle kernels each modeled as a radially symmetric ($\lambda_2 = \lambda_3$) diffusion tensor. The putative kernels are distributed in a dense sampling grid on the sphere. Furthermore, Restriction Spectrum Imaging (RSI (White et al., 2013)) is used to extend the model, by adding a range of fascicle kernels in each sampling point, with different axial and radial diffusivities, capturing diffusion at different scales. To restrict the number of anisotropic components (fascicles) in each voxel, and to prevent overfitting, the RS-SFM model employs the Elastic Net algorithm (EN (Zou and Hastie, 2005)), which applies a tunable combination of L1 and L2 regularization on the weights of the fascicle kernels. We used elements of the SFM implemented in the dipy software library (Garyfallidis et al., 2014) and the EN implemented in scikit-learn (Pedregosa et al., 2011). In addition, to account for differences in SNR, we implemented a weighted least-squares strategy whereby each signal’s contribution to the fit was weighted by its TE, as well as the gradient strength used. EN has two tuning parameters determining: 1) the ratio of L1-to-L2 regularization, and 2) the weight of the regularization relative to the least-squares fit to the signal. To find the proper values of these parameters, we employed k-fold cross-validation (Rokem et al., 2015), leaving out one shell of measurement in each iteration for cross-validation. We determined that the tuning parameters with the lowest LSE (Panagiotaki et al., 2012) provide an almost-even balance of L1 and L2 penalty with weak overall regularization. Because of the combination of a dense sampling grid (362 points distributed on the sphere), and multiple restriction kernels (45 per sampling point), the maximal number of parameters for the model is approximately 16,300, more than the number of data points. However, because regularization is employed, the effective number of parameters is much smaller, resulting in an active set of approximately 20 regressors (Zou et al., 2007). We have made code to fully reproduce our results available at <https://arokem.github.io/ISBI2015>.

7.1.7. Eufracio (CIMAT, Mexico): Diffusion Basis Functions for Multi-Shell Scheme

This model is based on the Diffusion Basis Functions (DBF) model (Ramirez-Manzanares et al., 2007), a discrete version of the Gaussian Mixture Model for the sphere: $\hat{s}_i = \sum_{j=1}^m \alpha_j \phi_{ij} + \epsilon$, with $\hat{s}_i = s_i/s_0$,

$\phi_{ij} = \exp(-bq_i^T T_j q_i)$ and $T_j = (\chi_1 v_j v_j^T + \chi_2 I)$. The DBF model is reformulated by substituting ϕ_{ij} and T_j : $\hat{s}_i = \sum_{j=1}^m \alpha_j \exp(-b_i \chi_2 g_i^T g_i) \exp(-b_i \chi_1 (v_j^T g_i)^2) + \epsilon$. The first exponential can be defined as a scale factor that depends on the b-values, $\beta_i = \exp(-b_i \chi_2 q_i^T q_i)$. In this way, the β_i factors are associated with different b-values, so the new model includes the information of multi-shell schemes. The coefficients α and the shell scale factor β are computed by solving the optimisation problem:

$$\min_{\alpha, \beta_c} f(\alpha, \beta_c; \lambda_\alpha, \lambda_\beta) = \|B\tilde{\Phi}\alpha - S\|_2^2 + \lambda_\alpha \|\alpha\|_1 + \lambda_\beta \|\beta_c^0 - \beta_c\|_2^2 \quad \text{s.t. } \mathbf{1}^T \alpha = 1, \alpha \geq 0 \quad (6)$$

where $B = \text{diag}(\beta_c)$, $\beta_c = \frac{1}{\#C} \sum_{i \in C} \exp(-b_i \chi_2 (q_i^T q_i))$ and C is the set of indices grouped by different b-values (and $\#C$ is the number of elements in it). The regularization term weighted by λ_α demands sparseness and the term weighted by λ_β prevents an over-fitting. The problem in eq.(6) is solved in three steps. First, the active atoms are predicted ($\alpha_i > 0$) with $\tilde{\alpha} = \text{argmin}_\alpha f(\alpha, \beta_c; \lambda_\alpha, \lambda_\beta)$. Second, the active atoms are corrected with $\alpha = \text{argmin}_{\{\alpha_i\}: \tilde{\alpha}_i > 0} f(\alpha, \beta_c; 0, \lambda_\beta)$. Finally, the factors β_c are updated with $\beta_c = \text{argmin}_{\beta_c} f(\alpha, \beta_c; \lambda_\alpha, \lambda_\beta)$. To solve each step, the active sets algorithm for quadratic programming is used.

To train the model for the WMM'15 data, eq.6 is solved for each voxel with the training data to find the optimal weights α_j and scale factors β_c that best reproduce the training data. For this challenge, the β_c factors are grouped by the 36 training shells and the method parameters are set by hand: $\lambda_\alpha = 0.5$, $\lambda_\beta = 0.02$, $\chi_1 = 9.5 \times 10^{-4}$ and $\chi_2 = 5 \times 10^{-5}$. To predict the unseen signal at each voxel, the reformulated model is used with the optimal weights α_j and the 12 scale factors for the unseen β_c are calculated by interpolation with the 36 optimal β_c of the training data.

7.1.8. Loya-Olivas_1 and Loya-Olivas_2 (CIMAT, Mexico): Linear Acceleration of Sparse and Adaptive Diffusion Dictionary (LASADD)

LASADD is a multi-tensor based technique to adapt dynamically the Diffusion Functions (DFs) dictionary to a DW-MRI signal (Loya-Olivas et al., 2015; Loya, 2015). The method changes size and orientation of relevant Diffusion Tensors (DTs). The optimisation algorithm uses a special DT expression and assumptions to reduce the computational cost.

The one-compartment version (LASADD-1C) is based on DBF multi-tensor model (Ramirez-Manzanares et al., 2007): $s_i^* = \sum_{j=1}^n \alpha_j \phi_{i,j}$ where $s_i^* = \frac{s_i}{s_{0i}}$, $\phi_{i,j} = \exp(-b_i \mathbf{g}_i^T \mathbf{T}_j \mathbf{g}_i)$, $\alpha_j > 0$, and $\sum_{j=1}^n \alpha_j = 1$. LASADD expresses the DT as

$$\mathbf{T}_j = \chi_{1j} \mathbf{v}_j \mathbf{v}_j^T + \chi_{2j} \mathbf{I}, \quad (7)$$

where $\chi_{\{1,2\}j}$ are scalars associated to the eigenvalues, \mathbf{v}_j is the Principal Diffusion Direction (PDD), and \mathbf{I} is the identity matrix. The algorithm iterates three steps, like Aranda et al. (2015a,b): Predict, Correct, and Generate, until convergence. Prediction selects the relevant DFs using LASSO to regulate the number

to choose. Correction adjusts volume fraction, size, and orientation of the DTs. Taking advantage of DT expression and Taylor first order series approximation of the exponential, the optimisations are reduced to bounded Least Squares problems which are solved by a Projected Gauss-Seidel scheme. Generation controls the overestimation of fibers by adding to the basis the resulted DTs of combining two and three DFs for the new iteration.

An extra refinement to the computed results, named LASADD-3C, splits each detected DF into three compartments (Sherbondy et al., 2010): intracellular (IC), extracellular (EC) and CSF. The multi-tensor model is $s_i^* = \sum_{j=1}^n \alpha_j^{IC} \psi_{i,j} + \sum_{j=1}^n \alpha_j^{EC} \theta_{i,j} + \alpha^{CSF} \omega_i$ with $\sum_{j=1}^n (\alpha_j^{IC} + \alpha_j^{EC}) + \alpha^{CSF} = 1$. The $\psi_{i,j}$ models the directional IC compartment diffusion for each fiber bundle using $\mathbf{T}_j^{IC} = \chi_{0j} \mathbf{v}_j \mathbf{v}_j^T$. The EC compartment with hindered diffusion uses the representation (7) for $\theta_{i,j}$. The isotropic diffusion ω_i uses $\mathbf{T}^{CSF} = \chi_3 \mathbf{I}$. This stage keeps fixed the PDDs and only adjust the α 's and χ 's of the three compartments.

The parameters of the models were estimated using the training dataset: the b values using the equation by Stejskal and Tanner (1965) and the S_0 values as the median of the gradient-free signals with equal echo time per voxel. The initial basis comprises 33 PDDs distributed in the unitary sphere. The bounds $\chi_{\{0,1\}} \in [1, 39] \times 10^{-4}$ and $\chi_{\{2,3\}} \in [1, 9] \times 10^{-4} \text{mm}^2/\text{s}$ and the LASSO regularisation parameter (equals 1.7) were tuned by hand such that provides the minimum error. The best multi-tensorial model for both algorithms was used for each voxel to predict the corresponding unseen data.

7.2. Signal models

7.2.1. Alipoor (Chalmers, Sweden)

The DMRI signal is modeled as a fourth-order symmetric tensor as proposed by (Özarslan and Mareci, 2003). Let $\mathbf{g}_i = [x_i \ y_i \ z_i]$ and $\mathbf{a}_i = [z_i^4 \ 4y_i z_i^3 \ 6y_i^2 z_i^2 \ 4y_i^3 z_i \ y_i^4 \ 4x_i z_i^3 \ 12x_i y_i z_i^2 \ 12x_i y_i^2 z_i \ 4x_i y_i^3 \ 6x_i^2 z_i^2 \ 12x_i^2 y_i z_i \ 6x_i^2 y_i^2 \ 4x_i^3 z_i \ 4x_i^3 y_i \ x_i^4]^T$ be a gradient encoding direction and corresponding design vector, respectively. The diffusion signal is then described by

$$S(\mathbf{g}_i) = S_0 \exp\left(\frac{-TE}{T_2}\right) \exp(-\mathbf{b}\mathbf{t}^T \mathbf{a}_i) \quad (8)$$

where $S(\mathbf{g}_i)$ is the measured signal when the diffusion sensitizing gradient is applied in the direction \mathbf{g}_i , S_0 is the observed signal in the absence of such a gradient, b is the diffusion weighting factor, and $\mathbf{t} \in \mathbb{R}^{15}$ contains the distinct entries of a fourth-order symmetric tensor. Note that $d(\mathbf{g}_i, \mathbf{t}) = d(\mathbf{g}_i)$ is used for simplification. Given measurements in $N > 15$ different directions, the least squares (LS) estimate of the diffusion tensor is $\hat{\mathbf{t}} = (\mathbf{G}^T \mathbf{G})^{-1} \mathbf{G}^T \mathbf{y}$ where \mathbf{G} is an $N \times 15$ matrix defined $\mathbf{G} = [\mathbf{a}_1 \ \mathbf{a}_2 \ \dots \ \mathbf{a}_N]^T$ and $y_i = -b^{-1} \ln(S(\mathbf{g}_i)/S_0)$. We use the weighted LS tensor estimation method in (Alipoor et al., 2013) to mitigate the influence of outliers.

To estimate the diffusion signal for a given acquisition protocol with $TE = TE_x$, $b = b_x$ and $\delta = \delta_x$, the two non-diffusion weighted measurements with the closest TE s to TE_x (among measurements with $\delta = \delta_x$) are

used to estimate T_2 and S_0 for each voxel. Then, data from the closet shell to b_x (among shells with $\delta = \delta_x$) are used to estimate the tensor describing the underlying structure.

7.2.2. Sakaie-Tatsuoka-Ghosh (Cleveland, USA): An Empirical Approach

As the extent of q-space in the dataset is unusually comprehensive, we chose a simple, generic approach to gain intuition. Visual inspection suggested use of a restricted and hindered component each with angular variation:

$$S_i = A_{TE_i}(fR_i + (1 - f)\exp(-b_iD_i)) \quad (9)$$

where S_i is the predicted signal for signal acquired with TE_i , b_i . A_{TE_i} is the median signal at a given TE with no diffusion weighting. Fit parameters are f , the volume fraction of R_i , the restricted component, and D_i , the diffusivity. R_i and D_i are modeled as spherical harmonics with real, antipodal symmetry (Alexander et al., 2002) with maximum degree 4. The model has 31 fit parameters for each voxel. Data were fit using using a nonlinear least squares algorithm (lsqcurvefit, MATLAB). Prior to the fit, data points with nonzero bvalue that had signal higher than the the median of the b=0 signal plus 1.4826 times the median absolute deviation were excluded. Shells with normalized median signal smaller than that of shells with lower bvalues were also excluded. Normalization was performed by dividing by the median of the b=0 signal with the same TE.

7.2.3. Fick (INRIA, France): A Spatio-Temporal Functional Basis to Represent the Diffusion MRI Signal

We use our recently proposed spatio-temporal (3D+t) functional basis (Fick et al., 2015) to simultaneously represent the diffusion MRI signal over three-dimensional wave vector \mathbf{q} and diffusion time τ . Based on Callaghan’s theoretical model of spatio-temporal diffusion in pores (Callaghan, 1995), our basis represents the 3D+t diffusion signal attenuation $E(\mathbf{q}, \tau)$ as a product of a spatial and temporal functional basis as

$$E(\mathbf{q}, \tau) = \sum_{N=0}^{N_{\max}} \sum_{\{jlm\}} \sum_{o=0}^{O_{\max}} c_{\{jlm\}o} S_{jlm}(\mathbf{q}, u_s) T_o(\tau, u_t) \quad (10)$$

where T_o is our temporal basis with basis order o and S_{jlm} is the spatial isotropic MAP-MRI basis (Özarslan et al., 2013) with radial and angular basis orders j , l and m . Here N_{\max} and O_{\max} are the maximum spatial and temporal order of the bases, which can be chosen independently. We formulate the bases themselves as

$$\begin{aligned} S_{jlm}(\mathbf{q}, u_s) &= \sqrt{4\pi} i^{-l} (2\pi^2 u_s^2 q^2)^{l/2} e^{-2\pi^2 u_s^2 q^2} L_{j-1}^{l+1/2}(4\pi^2 u_s^2 q^2) Y_l^m(\mathbf{u}) \\ T_o(\tau, u_t) &= \exp(-u_t \tau / 2) L_o(u_t \tau) \end{aligned} \quad (11)$$

with u_s and u_t the spatial and temporal scaling functions, Y_l^m the spherical harmonics and L_o a Laguerre polynomial. We calculate the spatial scaling u_s by fitting an isotropic tensor to the TE-normalized signal attenuation $E(\mathbf{q}, \cdot)$ for all \mathbf{q} . Similarly, we compute u_t by fitting an exponential $e^{-u_t \tau / 2}$ to $E(\cdot, \tau)$ for all τ . We fit our basis using Laplacian-regularized least squares in the following steps: We first denote

$\Xi_i(\mathbf{q}, \tau, u_s, u_t) = S_{jlm(i)}(\mathbf{q}, u_s)T_{o(i)}(\tau, u_t)$ with $i \in \{1 \dots N_{\text{coef}}\}$ with N_{coef} the number of fitted coefficients. We then construct a design matrix $\mathbf{Q} \in \mathbb{R}^{N_{\text{data}} \times N_{\text{coef}}}$ with $\mathbf{Q}_{ik} = S_{N_i}(\mathbf{A}, \mathbf{q}_k)T_{o_i}(\tau_k, u_t)$. The signal is then fitted as $\mathbf{c} = \text{argmin}_{\mathbf{c}} \|\mathbf{y} - \mathbf{Q}\mathbf{c}\|^2 + \lambda U(\mathbf{c})$ with \mathbf{y} the measured signal, \mathbf{c} the fitted coefficients and λ the weight for our analytic Laplacian regularization $U(\mathbf{c})$. We used generalized cross-validation (Craven and Wahba, 1978) to find the optimal regularization weighting λ in every voxel. In our submitted results, we used a spatial order of 8 and a temporal order of 4, resulting in 475 fitted coefficients.

7.2.4. Rivera (CIMAT, Mexico): Baseline Method: Robust Regression

We regard this very simplistic model as a baseline for other model-based methods. It assumes as little information as possible from the diffusion signal. The vector of independent variables is $x_i = [g_i, |G|_i, \Delta_i, \delta_i, TE_i, b_i]$, containing the gradient strength g , the echo time TE and the b-value b . Given signal s_i , we then estimate the parameters of the linear regression model:

$$s = X\theta + \epsilon \quad (12)$$

where $\theta \in \mathbb{R}^{23}$ is the unknown vector of coefficients, ϵ is the residual error and

$$X = [x, x^2, \Delta \delta, \Delta TE, \Delta b, \delta TE, \delta b, TE b, 1]$$

is the *matrix design* (x^2 is obtained from squaring each element of the matrix x). To account for outliers we estimate θ with a weighted (robust) least squares approach using the Lasso Regularization:

$$\theta^{t+1} = \text{argmin}_{\theta} \|W^t(X\theta - y)\|_2^2 + \lambda \|\theta\|_1 \quad (13)$$

where W^0 is the identity matrix and each subsequent W computed via:

$$W^{t+1} = \text{diag}(v_i^{t+1} w_i^{t+1}) \quad (14)$$

with outlier weighting in $\omega_i^{t+1} = \kappa^2 / (\kappa^2 + (y_i - X\theta_i^{t+1})^2)$ though κ , an arbitrary parameter that controls the outlier sensitivity. The protocol weight

$$v_i^{t+1} = \text{mean}_{j \in \Omega_i} \{w_j^{t+1}\} \text{ and } \Omega_i = \{j : TE_j = TE_i, |G_j| = |G_i|\} \quad (15)$$

computes a confidence factor for the complete protocol.

The equations (13) and (14) are iterated three times. The final estimated signal is computed using (12), using the protocol of the unseen signal.

References

References

Alexander, D., Barker, G., Arridge, S., 2002. Detection and modeling of non-Gaussian apparent diffusion coefficient profiles in human brain data. *Magnetic Resonance in Medicine* 48, 331–340.

- Alexander, D.C., 2005. Maximum entropy spherical deconvolution for diffusion MRI, in: *Biennial International Conference on Information Processing in Medical Imaging*, Springer. pp. 76–87.
- Alexander, D.C., Hubbard, P.L., Hall, M.G., Moore, E.A., Ptito, M., Parker, G.J., Dyrby, T.B., 2010. Orientationally invariant indices of axon diameter and density from diffusion MRI. *NeuroImage* 52, 1374–1389.
- Alipoor, M., Gu, I.Y., Mehnert, A.J., Lilja, Y., Nilsson, D., 2013. On high order tensor-based diffusivity profile estimation, in: *Engineering in Medicine and Biology Society (EMBC), 2013 35th Annual International Conference of the IEEE*, pp. 93–96.
- Anderson, A.W., 2005. Measurement of fiber orientation distributions using high angular resolution diffusion imaging. *Magnetic Resonance in Medicine* 54, 1194–1206.
- Aranda, R., Ramirez-Manzanares, A., Rivera, M., 2015a. Recovering Detailed intra-voxel White Matter Structure by using an Adaptive Diffusion Dictionary, Presented in the ISMRM 23rd Annual Meeting and Exhibition, Toronto, Ontario, Canada.
- Aranda, R., Ramirez-Manzanares, A., Rivera, M., 2015b. Sparse and Adaptive Diffusion Dictionary (SADD) for recovering intra-voxel white matter structure. *Medical Image Analysis* 26, 243–255.
- Assaf, Y., Basser, P.J., 2005. Composite hindered and restricted model of diffusion (CHARMED) MR imaging of the human brain. *NeuroImage* 27, 48–58.
- Assaf, Y., Pasternak, O., 2008. Diffusion tensor imaging (DTI)-based white matter mapping in brain research: a review. *Journal of Molecular Neuroscience : MN* 34, 51–61.
- Assemlal, H.E., Tschumperlé, D., Brun, L., 2009. Efficient and robust computation of pdf features from diffusion MR signal. *Medical Image Analysis* 13, 715–729.
- Axer, H., Axer, M., Krings, T., Graf Diedrich v. Keyserlingk, D., 2001. Quantitative estimation of 3-d fiber course in gross histological sections of the human brain using polarized light. *Journal of Neuroscience Methods* 105, 121–131.
- Barazany, D., Basser, P.J., Assaf, Y., 2009. In vivo measurement of axon diameter distribution in the corpus callosum of rat brain. *Brain* 132, 1210–1220.
- Basser, P.J., Mattiello, J., LeBihan, D., 1994. Estimation of the effective self-diffusion tensor from the NMR spin echo. *Journal of Magnetic Resonance, Series B* 103, 247–254.
- Behrens, T., Berg, H.J., Jbabdi, S., Rushworth, M., Woolrich, M., 2007. Probabilistic diffusion tractography with multiple fibre orientations: What can we gain? *NeuroImage* 34, 144–155.
- Behrens, T., Woolrich, M., Jenkinson, M., Johansen-Berg, H., Nunes, R., Clare, S., Matthews, P., Brady, J., Smith, S., 2003. Characterization and propagation of uncertainty in diffusion-weighted MR imaging. *Magnetic Resonance in Medicine* 50, 1077–1088.
- Bron, E.E., Smits, M., van der Flier, W.M., Vrenken, H., Barkhof, F., Scheltens, P., Papma, J.M., Steketee, R.M., Orellana, C.M., Meijboom, R., et al., 2015. Standardized evaluation of algorithms for computer-aided diagnosis of dementia based on structural MRI: The caddementia challenge. *NeuroImage* 111, 562–579.
- Callaghan, P.T., 1995. Pulsed-gradient spin-echo nmr for planar, cylindrical, and spherical pores under conditions of wall relaxation. *Journal of Magnetic Resonance, Series A* 113, 53–59.
- Chenouard, N., Smal, I., et al., 2014. Objective comparison of particle tracking methods. *Nature Methods* 11, 281–289.
- Craven, P., Wahba, G., 1978. Smoothing noisy data with spline functions. *Numerische Mathematik* 31, 377–403.
- Daducci, A., Canales-Rodriguez, E.J., Descoteaux, M., Garyfallidis, E., Gur, Y., Lin, Y.C., Mani, M., Merlet, S., Paquette, M., Ramirez-Manzanares, A., et al., 2014. Quantitative comparison of reconstruction methods for intra-voxel fiber recovery from diffusion MRI. *Medical Imaging, IEEE Transactions on* 33, 384–399.
- Dell’Acqua, F., Rizzo, G., Scifo, P., Clarke, R.A., Scotti, G., Fazio, F., 2007. A model-based deconvolution approach to solve fiber crossing in diffusion-weighted mr imaging. *IEEE Transactions on Biomedical Engineering* 54, 462–472.
- Descoteaux, M., Angelino, E., Fitzgibbons, S., Deriche, R., 2007. Regularized, fast, and robust analytical Q-ball imaging. *Magnetic Resonance in Medicine* 58, 497–510.

- Duval, T., McNab, J., Setsompop, K., Witzel, T., Schneider, T., Susie Yi, H., Keil, B., Klawitter, E., Wald, L., Cohen-Adad, J., 2014. In vivo estimation of axon diameter in the human spinal cord using 300 mT/m gradients., in: Joint Annual Meeting ISMRM-ESMRMB 2014, Milan, Italy.
- Dyrby, T.B., Hall, M.G., Ptito, M., Alexander, D., et al., 2013. Contrast and stability of the axon diameter index from microstructure imaging with diffusion MRI. *Magnetic Resonance in Medicine* 70, 711–721.
- Efron, B., 1979. Bootstrap methods: another look at the jackknife. *The annals of Statistics* , 1–26.
- Ferizi, U., 2014. Compartment models and model selection for in-vivo diffusion-MRI of human brain white matter. Ph.D. thesis. University College London.
- Ferizi, U., Schneider, T., Panagiotaki, E., Nedjati-Gilani, G., Zhang, H., Wheeler-Kingshott, C.A., Alexander, D.C., 2014. A ranking of diffusion MRI compartment models with in vivo human brain data. *Magnetic Resonance in Medicine* 72, 1785–1792.
- Ferizi, U., Schneider, T., Tariq, M., Wheeler-Kingshott, C., Zhang, H., Alexander, D., 2013. The importance of being dispersed: A ranking of diffusion MRI models for fibre dispersion using in vivo human brain data, in: Mori, K., Sakuma, I., Sato, Y., Barillot, C., Navab, N. (Eds.), *Medical Image Computing and Computer-Assisted Intervention MICCAI 2013*. Springer Berlin Heidelberg. volume 8149 of *Lecture Notes in Computer Science*, pp. 74–81.
- Ferizi, U., Schneider, T., Zhang, H., Wheeler-Kingshott, C.A., Alexander, D.C., 2015. White matter compartment models for in vivo diffusion MRI at 300 mt/m. *NeuroImage* .
- Fick, R., Wassermann, D., Pizzolato, M., Deriche, R., 2015. A unifying framework for spatial and temporal diffusion in diffusion mri, in: *International Conference on Information Processing in Medical Imaging*, Springer. pp. 167–178.
- Fieremans, E., Jensen, J.H., Helpert, J.A., 2011. White matter characterization with diffusional kurtosis imaging. *Neuroimage* 58, 177–188.
- Fillard, P., Descoteaux, M., Goh, A., Gouttard, S., Jeurissen, B., Malcolm, J., Ramirez-Manzanares, A., Reisert, M., Sakaie, K., Tensaouti, F., et al., 2011. Quantitative evaluation of 10 tractography algorithms on a realistic diffusion mr phantom. *Neuroimage* 56, 220–234.
- Garyfallidis, E., Brett, M., Amirbekian, B., Rokem, A., van der Walt, S., Descoteaux, M., Nimmo-Smith, I., Dipy Contributors, 2014. Dipy, a library for the analysis of diffusion MRI data. *Front. Neuroinform.* 8, 8.
- Ghosh, A., Zhang, H., Alexander, D.C., 2016. To be dispersed or not to be dispersed: A study using hcp data, in: *ISMRM Proceedings*.
- Hameeteman, K., Zuluaga, M.A., et al., 2011. Evaluation framework for carotid bifurcation lumen segmentation and stenosis grading. *Medical Image Analysis* 15, 477–488.
- Huang, S.Y., Nummenmaa, A., Witzel, T., Duval, T., Cohen-Adad, J., Wald, L.L., McNab, J.A., 2015. The impact of gradient strength on in vivo diffusion MRI estimates of axon diameter. *NeuroImage* 106, 464–472.
- Jbabdi, S., Sotiropoulos, S., Savio, A., Graa, M., Behrens, T., 2012. Model-based analysis of multishell diffusion MR data for tractography: How to get over fitting problems. *Magnetic Resonance in Medicine* 68, 1846–1855.
- Jelescu, I.O., Veraart, J., Adisetiyo, V., Milla, S.S., Novikov, D.S., Fieremans, E., 2015. One diffusion acquisition and different white matter models: how does microstructure change in human early development based on WMTI and NODDI? *NeuroImage* 107, 242–256.
- Jelescu, I.O., Veraart, J., Fieremans, E., Novikov, D.S., 2016. Degeneracy in model parameter estimation for multi-compartmental diffusion in neuronal tissue. *NMR in Biomedicine* 29, 33–47.
- Jenkinson, M., Bannister, P., Brady, M., Smith, S., 2002. Improved optimization for the robust and accurate linear registration and motion correction of brain images. *NeuroImage* 17, 825–841.
- Jensen, J.H., Helpert, J.A., Ramani, A., Lu, H., Kaczynski, K., 2005a. Diffusional kurtosis imaging: The quantification of non-gaussian water diffusion by means of magnetic resonance imaging. *Magnetic Resonance in Medicine* 53, 1432–1440.

- Jensen, J.H., Helpert, J.A., Ramani, A., Lu, H., Kaczynski, K., 2005b. Diffusional kurtosis imaging: The quantification of non-gaussian water diffusion by means of magnetic resonance imaging. *Magnetic Resonance in Medicine* 53, 1432–1440.
- Jian, B., Vemuri, B.C., 2007. Multi-fiber reconstruction from diffusion mri using mixture of wisharts and sparse deconvolution, in: *Information Processing in Medical Imaging*, Springer. pp. 384–395.
- Jian, B., Vemuri, B.C., Özarslan, E., Carney, P.R., Mareci, T.H., 2007. A novel tensor distribution model for the diffusion-weighted MR signal. *NeuroImage* 37, 164–176.
- Jones, D.K., Basser, P.J., 2004. “Squashing peanuts and smashing pumpkins”: How noise distorts diffusion-weighted MR data. *Magnetic Resonance in Medicine* 52, 979–993.
- Kaden, E., Kelm, N.D., Carson, R.P., Does, M.D., Alexander, D.C., 2016. Multi-compartment microscopic diffusion imaging. *NeuroImage* .
- Kaden, E., Kruggel, F., Alexander, D.C., 2015. Quantitative mapping of the per-axon diffusion coefficients in brain white matter. *Magnetic Resonance in Medicine* .
- Kiselev, V.G., 2011. The cumulant expansion: an overarching mathematical framework for understanding diffusion NMR. *Diffusion MRI: Theory, Methods, and Applications* , 152–168.
- Klein, A., Andersson, J., Ardekani, B.A., Ashburner, J., Avants, B., Chiang, M.C., Christensen, G.E., Collins, D.L., Gee, J., Hellier, P., et al., 2009. Evaluation of 14 nonlinear deformation algorithms applied to human brain MRI registration. *NeuroImage* 46, 786–802.
- Litjens, G., Toth, R., et al, 2014. Evaluation of prostate segmentation algorithms for MRI: the promise12 challenge. *Medical Image Analysis* 18, 359–373.
- Liu, C., Bammer, R., Moseley, M.E., 2003. Generalized diffusion tensor imaging (GDTI): A method for characterizing and imaging diffusion anisotropy caused by non-gaussian diffusion. *Israel Journal of Chemistry* 43, 145–154.
- Lo, P., Van Ginneken, B., Reinhardt, J.M., Yavarna, T., De Jong, P.A., Irving, B., Fetita, C., Ortner, M., Pinho, R., Sijbers, J., et al., 2012. Extraction of airways from ct (EXACT’09). *IEEE Transactions on Medical Imaging* 31, 2093–2107.
- Loya, A.K., 2015. Algoritmos para Solución de Modelos No Lineales en DW-MRI. Master’s thesis. Centro de Investigación en Matemáticas, A.C.
- Loya-Olivas, A., Aranda, R., Rivera, M., 2015. LASADD: Linear Acceleration Method for Adapting Diffusion Dictionaries, Presented in the ISMRM 23rd Annual Meeting and Exhibition, Toronto, Ontario, Canada.
- McNab, J.A., Edlow, B.L., Witzel, T., Huang, S.Y., Bhat, H., Heberlein, K., Feiweier, T., Liu, K., Keil, B., Cohen-Adad, J., et al., 2013. The human connectome project and beyond: Initial applications of 300mT/m gradients. *NeuroImage* 80, 234–245.
- Mendrik, A., Vincken, K., Kuijf, H., et al, 2015. MRBrainS challenge: Online evaluation framework for brain image segmentation in 3t MRI scans. *Computational Intelligence and Neuroscience* .
- Mitra, P.P., Sen, P.N., Schwartz, L.M., Le Doussal, P., 1992. Diffusion propagator as a probe of the structure of porous media. *Physical Review Letters* 68, 3555.
- Murphy, K., Van Ginneken, B., Reinhardt, J.M., Kabus, S., Ding, K., Deng, X., Cao, K., Du, K., Christensen, G.E., Garcia, V., et al., 2011. Evaluation of registration methods on thoracic CT: the EMPIRE10 challenge. *Medical Imaging, IEEE Transactions on* 30, 1901–1920.
- Nilsson, M., Lätt, J., Ståhlberg, F., Westén, D., Hagslätt, H., 2012. The importance of axonal undulation in diffusion MR measurements: a monte carlo simulation study. *NMR in Biomedicine* 25, 795–805.
- Nilsson, M., van Westén, D., Ståhlberg, F., Sundgren, P.C., Lätt, J., 2013. The role of tissue microstructure and water exchange in biophysical modelling of diffusion in white matter. *Magnetic Resonance Materials in Physics, Biology and Medicine* 26, 345–370.
- Ning, L., Laun, F., Gur, Y., DiBella, E.V., Deslauriers-Gauthier, S., Megherbi, T., Ghosh, A., Zucchelli, M., Menegaz, G.,

- Fick, R., et al., 2015. Sparse reconstruction challenge for diffusion mri: Validation on a physical phantom to determine which acquisition scheme and analysis method to use? *Medical Image Analysis* 26, 316–331.
- Novikov D, Jelescu I, V.J.F.E., 2015. Lemonade: Linearly estimated moments provide orientations of neurites and diffusivities exactly., OHBM.
- Özarslan, E., Koay, C., Basser, P., 2008. Simple harmonic oscillator based estimation and reconstruction for one-dimensional q-space MR, in: *Proc. Intl. Soc. Mag. Reson. Med*, p. 35.
- Özarslan, E., Koay, C.G., Shepherd, T.M., Komlosh, M.E., İrfanoğlu, M.O., Pierpaoli, C., Basser, P.J., 2013. Mean apparent propagator (MAP) MRI: A novel diffusion imaging method for mapping tissue microstructure. *NeuroImage* 78, 16–32.
- Özarslan, E., Mareci, T.H., 2003. Generalized diffusion tensor imaging and analytical relationships between diffusion tensor imaging and high angular resolution diffusion imaging. *Magn Reson Med* 50, 955–965.
- Panagiotaki, E., Schneider, T., Siow, B., Hall, M.G., Lythgoe, M.F., Alexander, D.C., 2012. Compartment models of the diffusion MR signal in brain white matter: a taxonomy and comparison. *NeuroImage* 59, 2241–2254.
- Pedregosa, F., Varoquaux, G., Gramfort, A., Michel, V., Thirion, B., Grisel, O., Blondel, M., Prettenhofer, P., Weiss, R., Dubourg, V., et al., 2011. Scikit-learn: Machine learning in python. *The Journal of Machine Learning Research* 12, 2825–2830.
- Poot, D., Klein., S., 2015. Detecting statistically significant differences in quantitative MRI experiments, applied to diffusion tensor imaging. *IEEE T MED IMAGING* 34, 1164–1176.
- Price, S., Jena, R., Burnet, N., Hutchinson, P., Dean, A., Pena, A., Pickard, J., Carpenter, T., Gillard, J., 2006. Improved delineation of glioma margins and regions of infiltration with the use of diffusion tensor imaging: an image-guided biopsy study. *American journal of neuroradiology* 27, 1969–1974.
- Pujol, S., Wells, W., Pierpaoli, C., et al, 2015. The DTI challenge: Toward standardized evaluation of diffusion tensor imaging tractography for neurosurgery. *Journal of Neuroimaging* 25, 875–882.
- Ramirez-Manzanares, A., Rivera, M., Vemuri, B.C., Carney, P., 2007. Diffusion basis functions decomposition for estimating white matter intravoxel fiber geometry. *Medical Imaging, IEEE Transactions on* 26, 1091–1102.
- Rathi, Y., Michailovich, O., Laun, F., Setsompop, K., Grant, P.E., Westin, C.F., 2014. Multi-shell diffusion signal recovery from sparse measurements. *Medical Image Analysis* 18, 1143–1156.
- Rokem, A., Yeatman, J.D., Pestilli, F., Kay, K.N., Mezer, A., van der Walt, S., Wandell, B.A., 2015. Evaluating the accuracy of diffusion MRI models in white matter. *PLoS One* 10, e0123272.
- Rose, S.E., Chen, F., Chalk, J.B., Zelaya, F.O., Strugnell, W.E., Benson, M., Semple, J., Doddrell, D.M., 2000. Loss of connectivity in Alzheimer’s disease: an evaluation of white matter tract integrity with colour coded MR diffusion tensor imaging. *Journal of Neurology, Neurosurgery & Psychiatry* 69, 528–530.
- Rueda, S., Fathima, S., Knight, C.L., et al, 2014. Evaluation and comparison of current fetal ultrasound image segmentation methods for biometric measurements: a grand challenge. *IEEE Trans. Med. Im.* 33, 797–813.
- Sakaie, K.E., Lowe, M.J., 2007. An objective method for regularization of fiber orientation distributions derived from diffusion-weighted mri. *NeuroImage* 34, 169–176.
- Scherrer, B., Schwartzman, A., Taquet, M., Sahin, M., Prabhu, S.P., Warfield, S.K., 2015. Characterizing brain tissue by assessment of the distribution of anisotropic microstructural environments in diffusion-compartment imaging (DIAMOND). *Magnetic Resonance in Medicine* .
- Setsompop, K., Kimmlingen, R., Eberlein, E., Witzel, T., Cohen-Adad, J., McNab, J.A., Keil, B., Tisdall, M.D., Hoecht, P., Dietz, P., et al., 2013. Pushing the limits of in vivo diffusion MRI for the Human Connectome project. *NeuroImage* 80, 220–233.
- Sherbondy, A.J., Rowe, M.C., Alexander, D.C., 2010. Microtrack: An algorithm for concurrent projectome and microstructure estimation, in: Jiang, T., Navab, N., Pluim, J., Viergever, M. (Eds.), *Medical Image Computing and Computer-Assisted*

- Intervention MICCAI 2010. Springer Berlin Heidelberg. volume 6361 of *Lecture Notes in Computer Science*, pp. 183–190. doi:10.1007/978-3-642-15705-9_23.
- Sotiropoulos, S.N., Behrens, T.E., Jbabdi, S., 2012. Ball and rackets: inferring fiber fanning from diffusion-weighted MRI. *NeuroImage* 60, 1412–1425.
- Stanisz, G.J., Wright, G.A., Henkelman, R.M., Szafer, A., 1997. An analytical model of restricted diffusion in bovine optic nerve. *Magnetic Resonance in Medicine* 37, 103–111.
- Stejskal, E.O., Tanner, J.E., 1965. Spin diffusion measurements: Spin echoes in the presence of a time-dependent field gradient. *The Journal of Chemical Physics* 42.
- Stone, M., 1974. Cross-validated choice and assessment of statistical predictions. *Journal of the Royal Statistical Society. Series B (Methodological)* , 111–147.
- Tournier, J.D., Calamante, F., Gadian, D.G., Connelly, A., 2004. Direct estimation of the fiber orientation density function from diffusion-weighted MRI data using spherical deconvolution. *Neuroimage* 23, 1176–1185.
- Tuch, D.S., 2004. Q-ball imaging. *Magnetic Resonance in Medicine* 52, 1358–1372.
- Van Gelderen, P., DesPres, D., van Zijl, P., Moonen, C.T., 1994. Evaluation of restricted diffusion in cylinders. phosphocreatine in rabbit leg muscle. *Journal of Magnetic Resonance Series B* 103, 255–260.
- Vangelderren, P., DesPres, D., Vanzijl, P., Moonen, C., 1994. Evaluation of restricted diffusion in cylinders. phosphocreatine in rabbit leg muscle. *Journal of Magnetic Resonance, Series B* 103, 255–260.
- Werring, D., Brassat, D., Droogan, A., Clark, C., Symms, M., Barker, G., MacManus, D., Thompson, A., Miller, D., 2000. The pathogenesis of lesions and normal-appearing white matter changes in multiple sclerosis. *Brain* 123, 1667–1676.
- White, N.S., Leergaard, T.B., D’Arceuil, H., Bjaalie, J.G., Dale, A.M., 2013. Probing tissue microstructure with restriction spectrum imaging: Histological and theoretical validation 34, 327–346.
- Yablonskiy, D.A., Bretthorst, L.G., Ackerman, J.J., 2003. Statistical model for diffusion attenuated MR signal. *Magnetic Resonance in Medicine* 50, 664–669.
- Yablonskiy, D.A., Sukstanskii, A.L., 2010. Theoretical models of the diffusion weighted MR signal. *NMR in Biomedicine* 23, 661–681.
- Zhang, H., Schneider, T., Wheeler-Kingshott, C.A., Alexander, D.C., 2012. NODDI: Practical in vivo neurite orientation dispersion and density imaging of the human brain. *NeuroImage* 61, 1000–1016.
- Zou, H., Hastie, T., 2005. Regularization and variable selection via the elastic net. *J. R. Stat. Soc. Series B Stat. Methodol.* 67, 301–320.
- Zou, H., Hastie, T., Tibshirani, R., Others, 2007. On the “degrees of freedom” of the lasso. *Ann. Stat.* 35, 2173–2192.
-

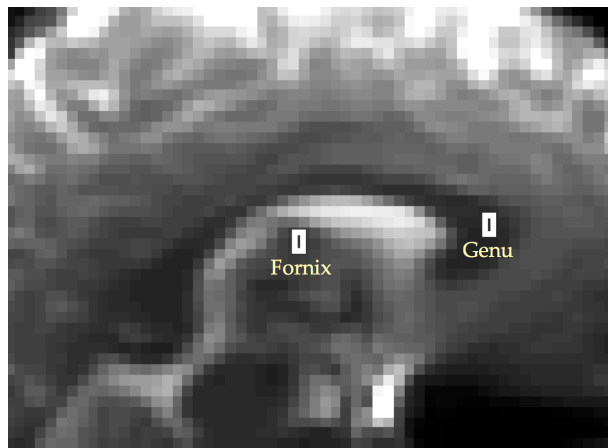


Figure 1:

Figure 2: We only consider two ROIs, each containing six voxels from the genu in the corpus callosum, where the fibres are approximately straight and parallel, and from the fornix, where the configuration of fibres is more complex.

Acquisition Protocol

	$\delta = 3ms$					$\delta = 8ms$				
	Nr	Δ (ms)	TE (ms)	$ G $ (mT/m)	b (s/mm ²)	Nr	Δ (ms)	TE (ms)	$ G $ (mT/m)	b (s/mm ²)
	1	22	49	61	50	25	22	58	58	300
	2	22	49	86	100	26	22	58	95	800
	3	22	49	192	500	27	22	58	190	3,200
	4	22	49	285	1,100	28	22	58	275	6,700
	5	40	67	63	100	29	40	72	59	600
	6	40	67	100	250	30	40	72	100	1,700
	7	40	67	200	1,000	31	40	72	200	6,850
	8	40	67	289	2,100	32	40	72	292	14,550
	9	60	87	63	150	33	60	92	34	300
	10	60	87	103	400	34	60	92	100	2,650
	11	60	87	199	1,500	35	60	92	200	10,500
	12	60	87	290	3,200	36	60	92	292	22,350
	13	80	107	63	200	37	80	112	61	1,300
	14	80	107	99	500	38	80	112	100	3,550
	15	80	107	201	2,050	39	80	112	200	14,150
	16	80	107	291	4,300	40	80	112	292	30,200
	17	100	127	63	250	41	100	132	60	1,600
	18	100	127	101	650	42	100	132	100	4,450
	19	100	127	200	2,550	43	100	132	200	17,850
	20	100	127	291	5,400	44	100	132	292	38,050
	21	120	147	63	300	45	120	152	60	1,950
	22	120	147	99	750	46	120	152	100	5,350
	23	120	147	199	3,050	47	120	152	200	21,500
	24	120	147	291	6,500	48	120	152	292	45,900

Note: We provide signal for the parts of protocol marked in black. In red is the protocol for which the signal needs to be predicted.

Table 1: The scanning protocol used, acquired in ~ 8 hours over two non-stop sessions. The protocol has 48 shells, each with 45 unique gradient directions ('blip-up-blip-down').

	Type of model	Nb of free param. (genu/fornix)	Models effect of δ and Δ	Noise assumption	Optimization algorithm	Outliers strategy	Special signal prediction strategy
R-Manzanares	Tissue	N/A	Yes	Gaussian	weighted-LS bootstrapping	Yes	CV
Nilsson	Tissue	< 12/12	Yes	Gaussian	LM	Yes	CV
Scherrer	Tissue	10/16	No	Gaussian	Bobyqa	Yes	No
Ferizi.1	Tissue	< 12/12	Yes	approx.-Rician	LM	No	No
Ferizi.2	Tissue	< 10/10	Yes	approx.-Rician	LM	No	No
Alipoor	Signal	17/17	No	Gaussian	weighted-LS	Yes	No
Sakaie	Signal	N/A	No	Gaussian	nonlinear-LS	Yes	No
Rokem	Tissue	~ 20	No	Gaussian + Noise floor	Elastic net	No	CV
Eufracio	Tissue	7/7	No	Gaussian	bounded-LS Lasso, Ridge	No	No
Loya-Olivas.1	Tissue	11	No	Gaussian	bounded-LS & Lasso	No	No
Loya-Olivas.2	Tissue	5	No	Gaussian	bounded-LS	No	No
Poot	Signal	103	No	Rician	LM-like	No	No
Fick	Signal	475	Yes	Gaussian	Laplacian-reg-LS	No	partial-CV
Rivera	Signal	N/A	Yes	Gaussian	Weighted Lasso	Yes	CV

Table 2: Summary of the various diffusion models evaluated. Tissue models are models that include an explicit description of the underlying tissue microstructure with a multi-compartment approach. In contrast, signal models focus on describing the DW signal attenuation without explicitly describing the underlying tissue and rather correspond to a “signal processing” approach. (Abbreviations: LS=Least Squares, LM=Levenberg-Marquardt, CV=cross-validation, reg=regularized.)

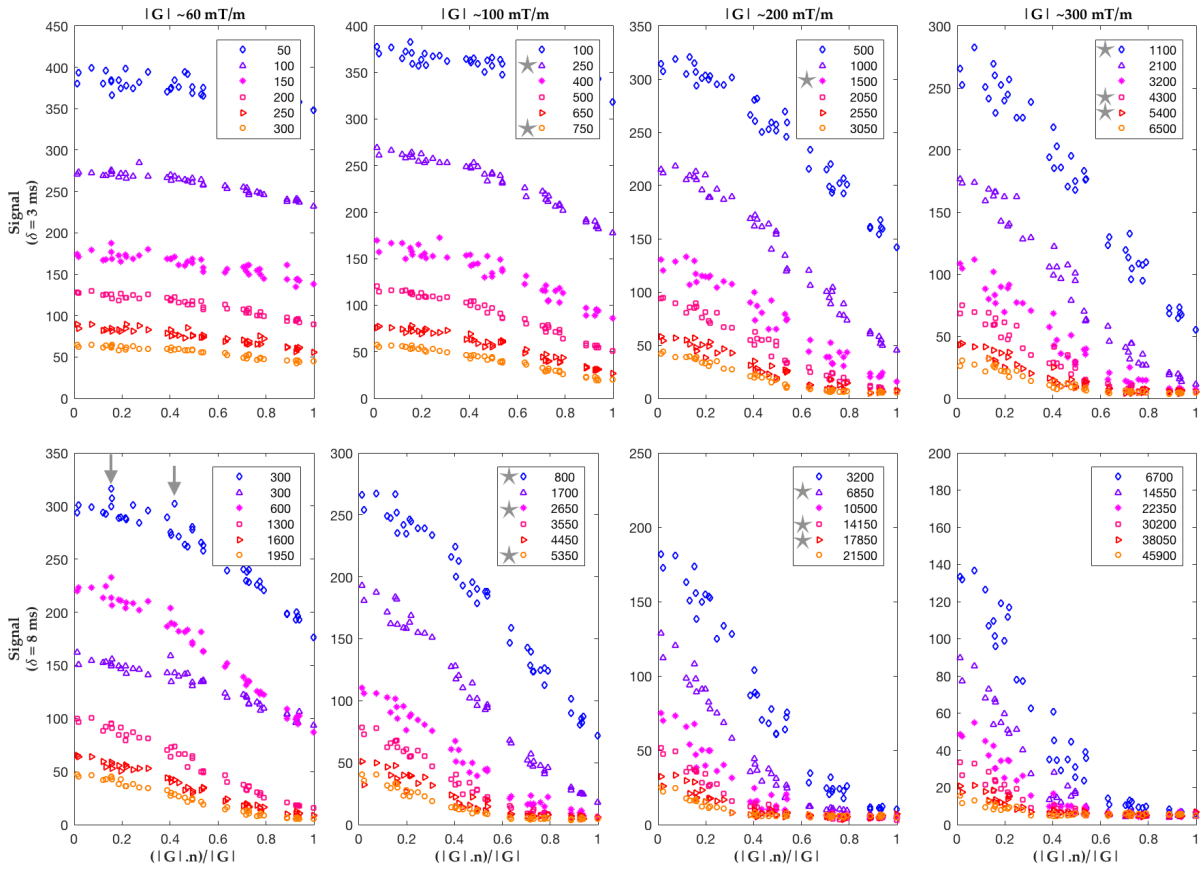


Figure 3:

Figure 4: Diffusion weighted signal from the genu ROI, averaged over the six voxels. Across each column and row, the signal pertains to one of the gradient strengths or pulse times δ used; while in each subplot, the six shells shown in different colours are Δ -specific, increasing in value (22, 40, 60, 80, 100, 120 ms) from top to bottom. Inside the legend, the b-value is in s/mm^2 units; here, the HARDI shells kept for testing are those marked with a star; the remaining shells comprise the training data. On the x-axis is the cosine of the angle between the applied diffusion gradient vector \mathbf{G} and the fibre direction \mathbf{n} . Some models in this study omit data outliers; two such data points are shown in the bottom-left subplot with vertical arrows — obviously each model has its own criteria for determining the outliers.

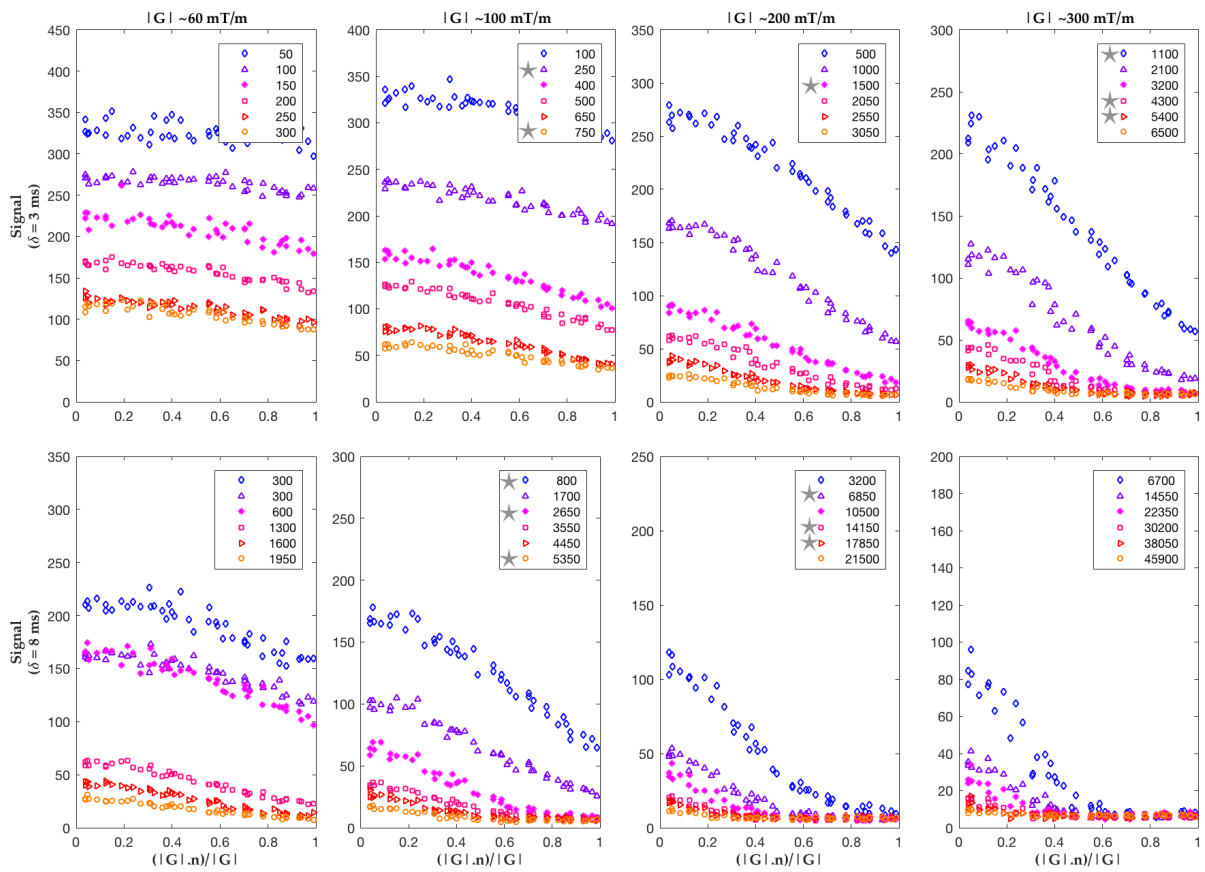


Figure 5:

Figure 6: Similar to Figure 4, here is the diffusion weighted signal from the fornix ROI, averaged over the six voxels.

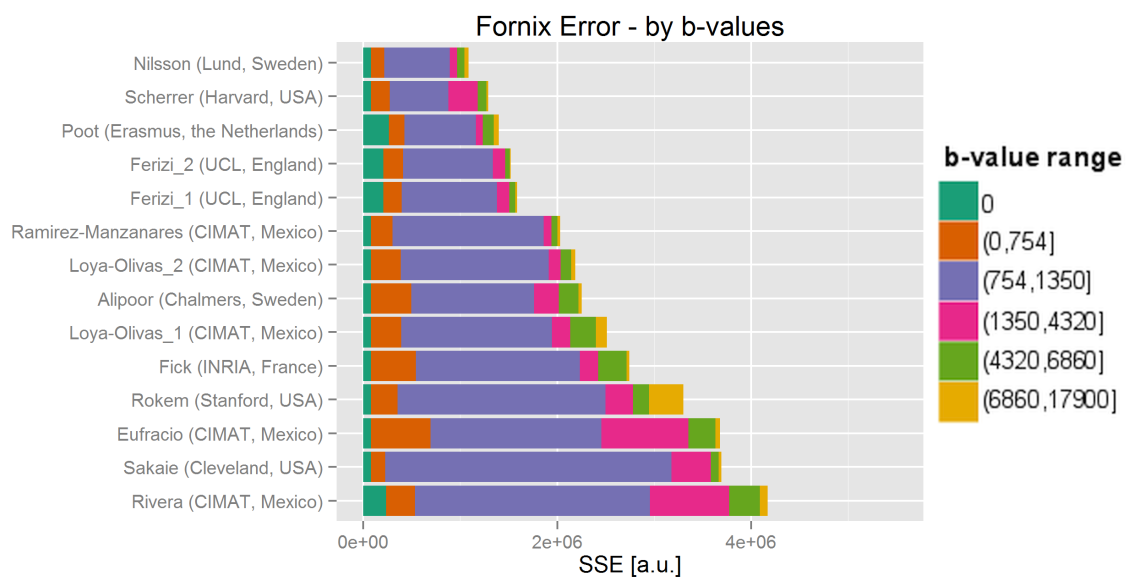
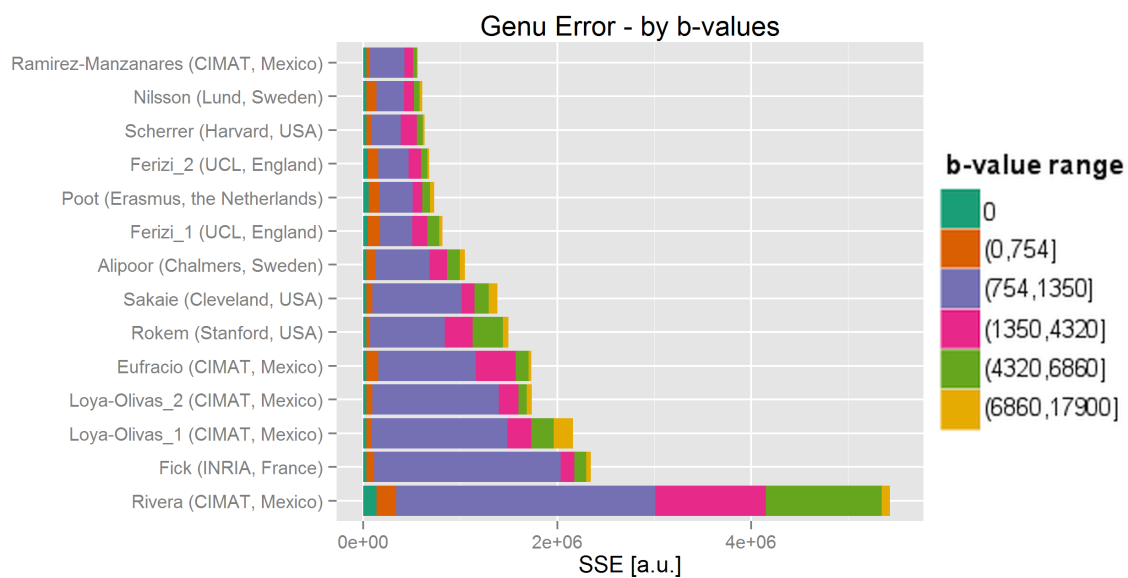


Figure 7:

Figure 8: Overall ranking of models by sum-of-squared-error metric over all voxels in genu (top) and fornix (bottom) ROIs. The colors represent different ranges of b-value shells.

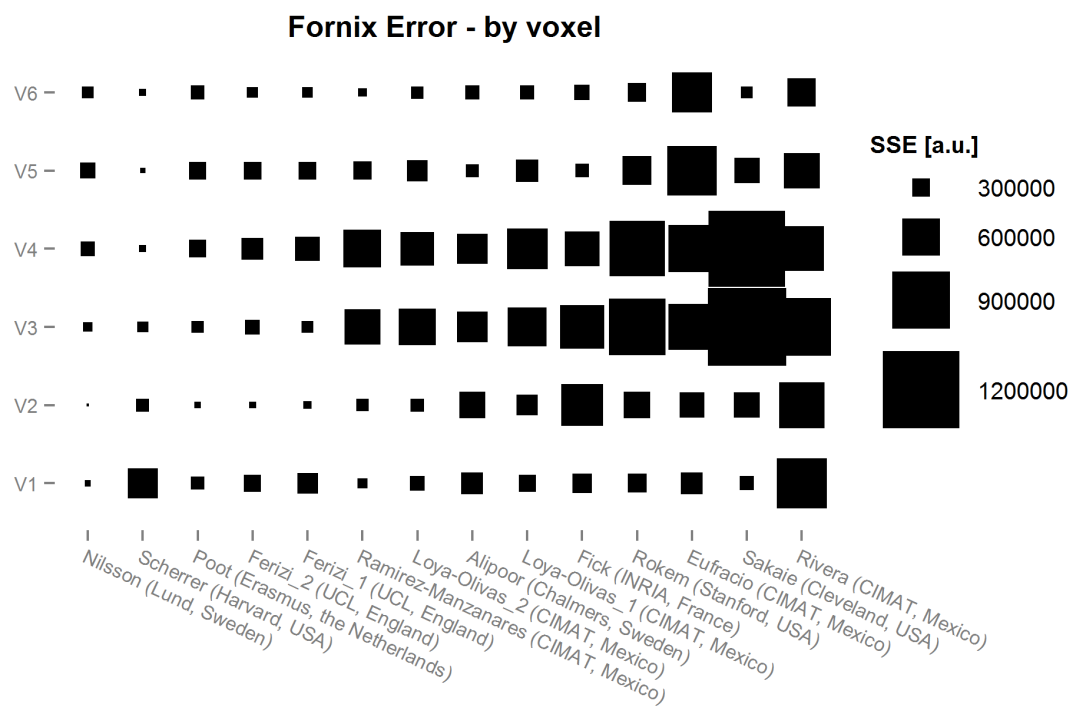
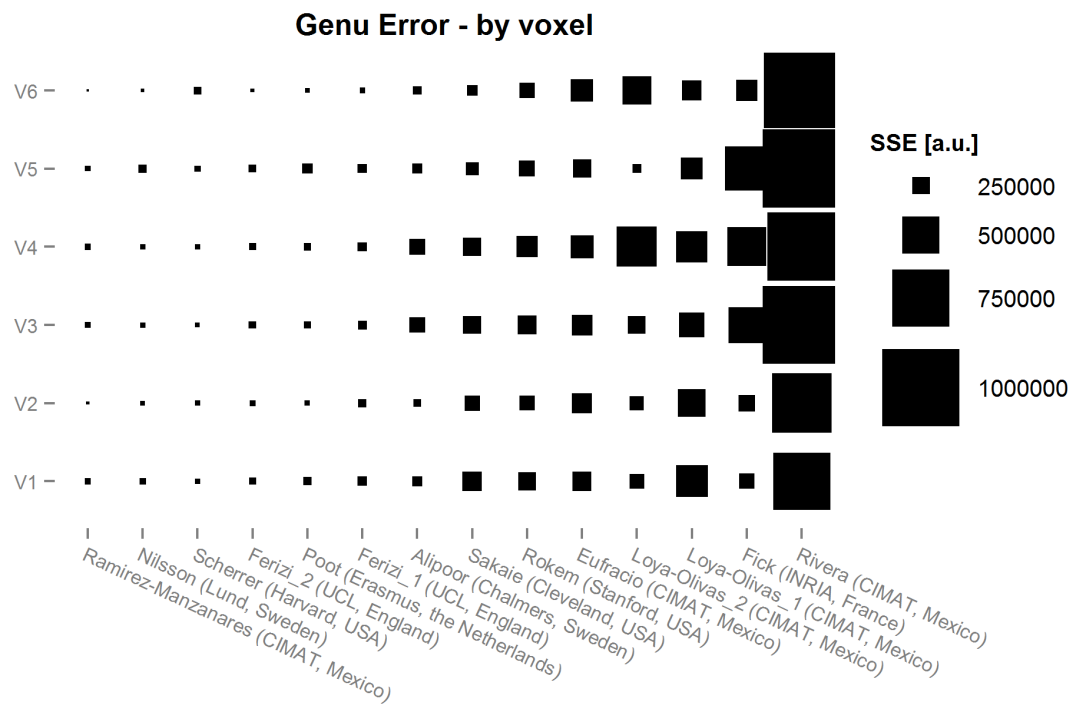


Figure 9:

Figure 10: Sum-of-squared-error per voxel for each model in genu and fornix. The size of rectangles represent the SSE value per voxel.

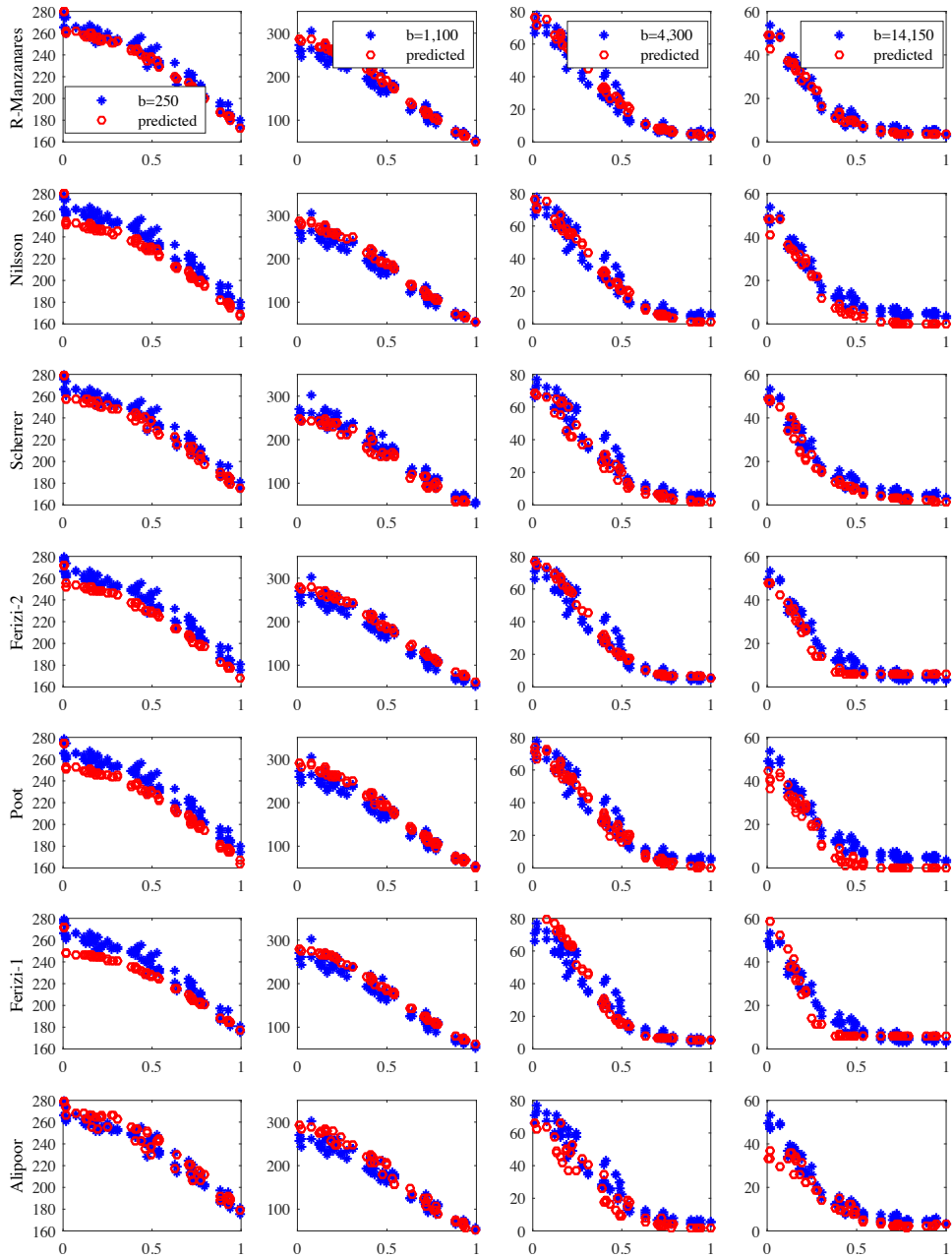


Figure 11:

Figure 12: An illustration of the observed and predicted genu signal of 7 of the 14 best models, shown in red circles, to 4 (of the total 12) representative shells, shown in blue stars. The best models are listed first. The axes are as in Fig.4.

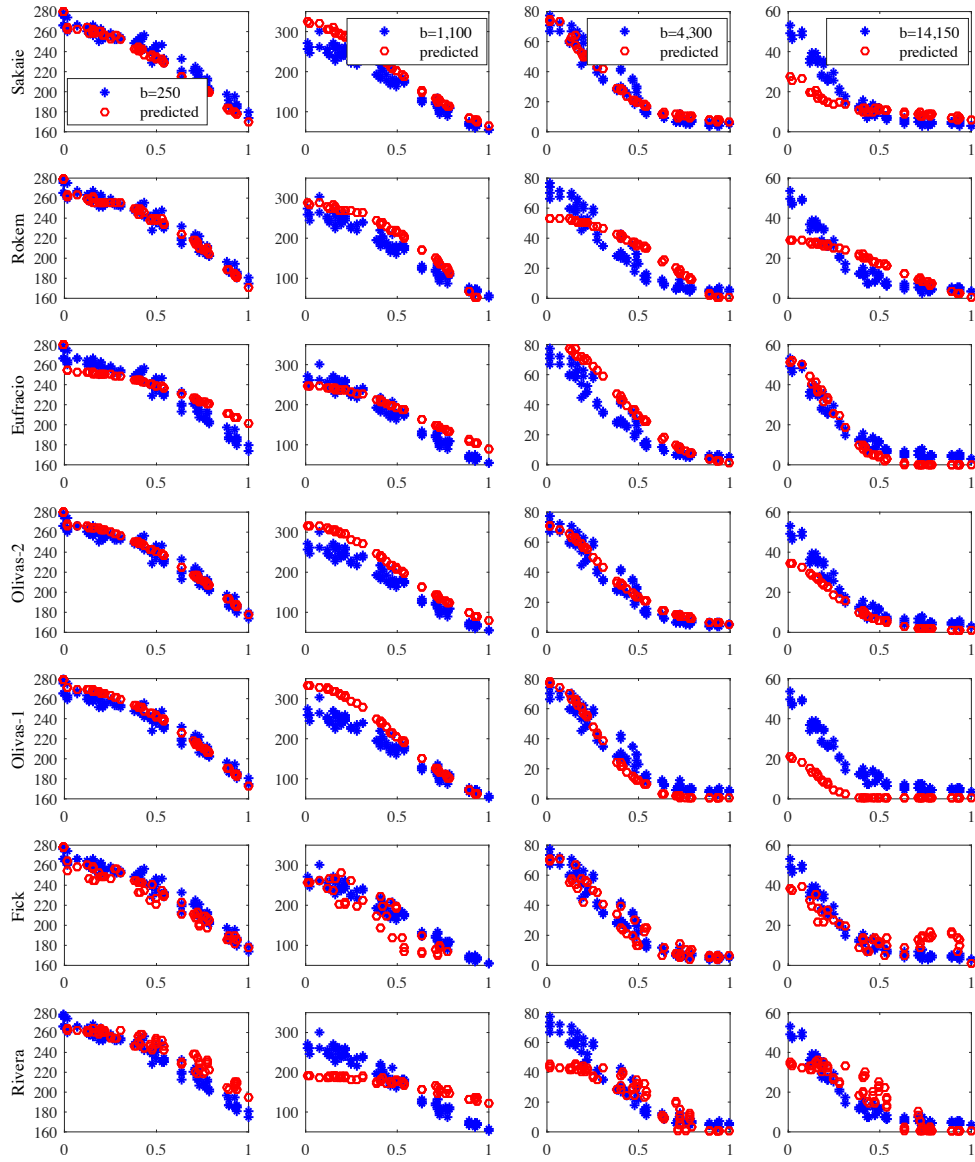


Figure 13:

Figure 14: Similar to Fig.12, here we show the remaining 7 model synthesized signals.